Cell Reports
Medicine

Article

AXL targeting restores PD-1 blockade sensitivity of *STK11/LKB1* mutant NSCLC through expansion of TCF1$^+$ CD8 T cells

Graphical abstract

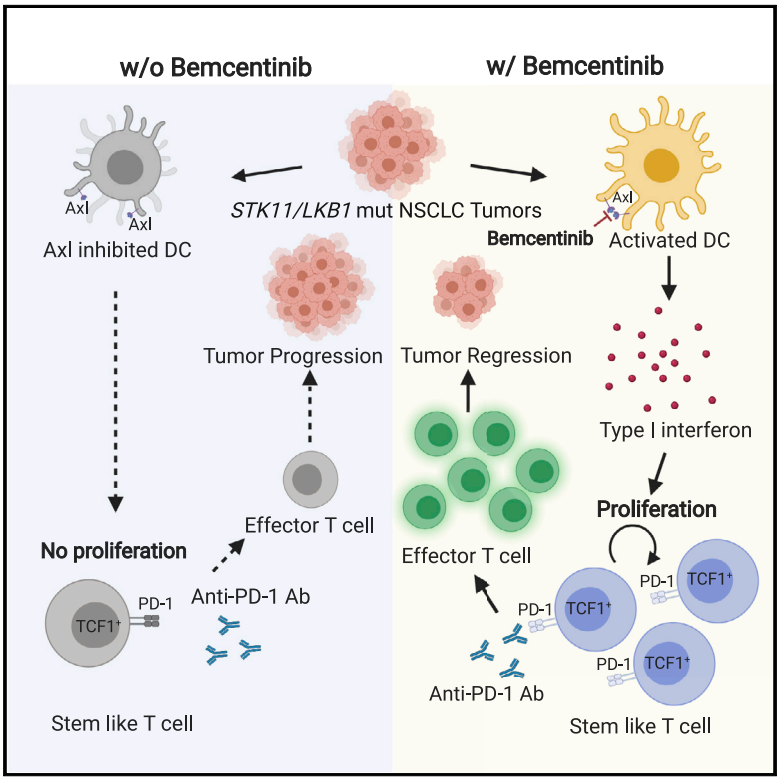

Highlights

- Lack of TCF1$^+$ CD8 T cells underlies poor response of *STK11* mutant NSCSLC to anti-PD-1
- Axl inhibition induces type I interferon and expansion of TCF1$^+$ CD8 T cells
- Axl inhibition sensitizes *STK11/LKB1* mutant NSCLC to anti-PD-1 therapy
- Preliminary clinical data supports inhibition of Axl and PD-1 in *STK11* mutant NSCLC

Authors

Huiyu Li, Zhida Liu, Longchao Liu, ..., Yang-Xin Fu, John D. Minna, Rolf A. Brekken

Correspondence

zhida_liu@saari.org.cn (Z.L.), yang-xin.fu@utsouthwestern.edu (Y.-X.F.), john.minna@utsouthwestern.edu (J.D.M.), rolf.brekken@utsouthwestern.edu (R.A.B.)

In brief

Li et al. provide mechanistic insight into why lung cancers with a common mutation (LKB1/STK11) are largely insensitive to immune therapy. The authors also demonstrate that inhibition of AXL activity in dendritic cells can restore sensitivity to immune therapy in LKB1/STK11 mutant lung cancer.

Li et al., 2022, Cell Reports Medicine *3*, 100554
March 15, 2022
https://doi.org/10.1016/j.xcrm.2022.100554

CellPress

Cell Reports Medicine

CellPress
OPEN ACCESS

Article

AXL targeting restores PD-1 blockade sensitivity of *STK11/LKB1* mutant NSCLC through expansion of TCF1^{+} CD8 T cells

Huiyu Li,[1,2] Zhida Liu,[3,16,*] Longchao Liu,[3] Hongyi Zhang,[4] Chuanhui Han,[3] Luc Girard,[1,13] Hyunsil Park,[1] Anli Zhang,[3] Chunbo Dong,[3] Jianfeng Ye,[4] Austin Rayford,[5,11] Michael Peyton,[1] Xiaoguang Li,[3] Kimberley Avila,[1] Xuezhi Cao,[3] Shuiqing Hu,[7] Md Maksudul Alam,[3] Esra A. Akbay,[3] Luisa M. Solis,[8] Carmen Behrens,[9] Sharia Hernandez-Ruiz,[8] Wei Lu,[8] Ignacio Wistuba,[8] John V. Heymach,[9] Michael Chisamore,[10] David Micklem,[5] Hani Gabra,[5] Gro Gausdal,[5] James B. Lorens,[11] Bo Li,[4,12] Yang-Xin Fu,[3,12,*] John D. Minna,[1,2,13,14,15,*] and Rolf A. Brekken[1,2,6,13,14,17,*]

[1]Hamon Center for Therapeutic Oncology Research, UT Southwestern Medical Center, 6000 Harry Hines Blvd., Dallas, TX 75390-8593, USA
[2]Cancer Biology Graduate Program, UT Southwestern Medical Center, Dallas, TX 75390, USA
[3]Department of Pathology, UT Southwestern Medical Center, 6000 Harry Hines Blvd., Dallas, TX 75390-9072, USA
[4]Lyda Hill Department of Bioinformatics, UT Southwestern Medical Center, Dallas, TX 75390, USA
[5]BerGenBio ASA, Bergen, Norway
[6]Department of Surgery, UT Southwestern Medical Center, Dallas, TX 75390, USA
[7]Department of Molecular Biology, UT Southwestern Medical Center, Dallas, TX 75390, USA
[8]Department of Translational Molecular Pathology, The University of Texas MD Anderson Cancer Center, Houston, TX 77030, USA
[9]Thoracic/Head and Neck Medical Oncology, The University of Texas MD Anderson Cancer Center, Houston, TX 77030, USA
[10]Merck & Co., Inc., Kenilworth, NJ 07033, USA
[11]Department of Biomedicine, Centre for Cancer Biomarkers, Norwegian Centre of Excellence, University of Bergen, Bergen, Norway
[12]Department of Immunology, UT Southwestern Medical Center, Dallas, TX 75390, USA
[13]Department of Pharmacology, UT Southwestern Medical Center, Dallas, TX 75390, USA
[14]Harold C. Simmons Comprehensive Cancer Center, UT Southwestern Medical Center, Dallas, TX 75390, USA
[15]Department of Internal Medicine, UT Southwestern Medical Center, Dallas, TX 75390, USA
[16]Present address: Shanxi Academy of Advanced Research and Innovation, 030032 Taiyuan, China
[17]Lead contact
*Correspondence: zhida_liu@saari.org.cn (Z.L.), yang-xin.fu@utsouthwestern.edu (Y.-X.F.), john.minna@utsouthwestern.edu (J.D.M.), rolf.brekken@utsouthwestern.edu (R.A.B.)
https://doi.org/10.1016/j.xcrm.2022.100554

SUMMARY

Mutations in *STK11/LKB1* in non-small cell lung cancer (NSCLC) are associated with poor patient responses to immune checkpoint blockade (ICB), and introduction of a *Stk11/Lkb1* (*L*) mutation into murine lung adenocarcinomas driven by mutant *Kras* and *Trp53* loss (*KP*) resulted in an ICB refractory syngeneic *KPL* tumor. Mechanistically this occurred because *KPL* mutant NSCLCs lacked TCF1-expressing CD8 T cells, a phenotype recapitulated in human *STK11/LKB1* mutant NSCLCs. Systemic inhibition of Axl results in increased type I interferon secretion from dendritic cells that expanded tumor-associated TCF1^{+}PD-1^{+}CD8 T cells, restoring therapeutic response to PD-1 ICB in *KPL* tumors. This was observed in syngeneic immunocompetent mouse models and in humanized mice bearing *STK11/LKB1* mutant NSCLC human tumor xenografts. NSCLC-affected individuals with identified *STK11/LKB1* mutations receiving bemcentinib and pembrolizumab demonstrated objective clinical response to combination therapy. We conclude that AXL is a critical targetable driver of immune suppression in *STK11/LKB1* mutant NSCLC.

INTRODUCTION

Immune checkpoint blockade (ICB) therapy, especially anti-programmed cell death protein 1/programmed death-ligand 1 (PD-1/PD-L1) therapy, has revolutionized non-small cell lung cancer (NSCLC) treatment, with clinical trials showing significantly prolonged survival for responding subjects.[1,2] However, ICB-induced clinical and survival benefit is limited to ~20% of NSCLC-affected individuals due to multiple mechanisms of ICB resistance, most of which are unknown.[3,4]

Mutant KRAS-driven NSCLCs tend to have a higher response rate to PD-1/PD-L1 inhibition compared with KRAS *wild-type* (WT) NSCLCs.[5,6] However, when KRAS is co-mutated with *STK11/LKB1* (incidence rate ~11% in lung adenocarcinoma [LUAD]), responses to ICB are usually abrogated.[7–11] *STK11/LKB1* (*L*) is a tumor suppressor gene that encodes a master serine threonine kinase involved in cell growth, metabolism,

and polarity by interacting with multiple downstream mediators including AMPK.[12–14] Mutations in *KRAS* and *STK11/LKB1* (*KL*) correlate with a more immunosuppressive tumor microenvironment (TME), which may account for the limited response to anti-PD-1/PD-L1 treatment.[11,15,16] Therefore, strategies that sensitize *KL* and *L* mutant NSCLC to ICB therapy would provide a significant clinical impact.

Stem-like T cell factor 1 (TCF1) (encoded by *Tcf7*) expressing PD-1$^+$ CD8 T cells are a key cell population that respond to PD-1/PD-L1 blockade in the TME.[17–21] Existence of TCF1$^+$PD1$^+$CD8 T cells allows for the expansion of differentiated TCF1$^-$PD-1$^+$CD8 T cells in response to anti-PD-1/PD-L1 therapy, ultimately leading to tumor growth control. However, no pharmacologic agent has been shown to expand TCF1$^+$PD-1$^+$CD8 T cells effectively. Furthermore, the status of TCF1$^+$PD-1$^+$CD8 T cells in *STK11/LKB1* mutated NSCLC tumors has not been investigated.

Although ICB can reverse the exhaustion status of CD8 T cells in tumors, the activation and differentiation of tumor-specific CD8 T cells requires antigen presentation by antigen-presenting cells (APCs). Axl, a receptor tyrosine kinase, is an innate checkpoint regulating APC activation.[22–24] Activation of Axl on innate immune cells suppresses type I interferon production, a critical signaling pathway for priming and activating anti-tumor CD8 T cells.[25–29] Thus, Axl inhibition is an attractive strategy to potentially expand PD-1$^+$ tumor-specific T cells and improve ICB efficacy.[30]

We investigated the immune landscape of mutant *KRAS*-driven NSCLC with and without *STK11/LKB1* mutations and used mouse models of *KL* NSCLC to determine if Axl inhibition enhances the efficacy of anti-PD-1 therapy. We found that murine NSCLCs with mutant *Stk11/Lkb1* lack TCF1$^+$PD-1$^+$CD8 T cells and that this deficiency limits response to ICB. We further demonstrate that Axl inhibition facilitates the expansion of TCF1$^+$PD-1$^+$CD8 T cells by interrupting Axl function in a subset of APCs. These preclinical observations are being evaluated in a clinical trial testing the benefit of combining bemcentinib, an Axl inhibitor, with the anti-PD-1 antibody pembrolizumab in NSCLC-affected individuals, some of which harbor mutations in *STK11/LKB1*.

RESULTS

STK11/LKB1 mutated NSCLC lacks anti-PD-1 treatment-responsive T cells in the TME

To dissect the immune landscape of *STK11/LKB1* mutant NSCLC, we used an isogenic pair of syngeneic murine LUAD cell lines derived from a tumor arising in a mutant *Kras/Tp53* knockout genetically engineered mouse model (referred to as "KP" tumor cells). KP expresses *WT Stk11/Lkb1*, while KPL was CRISPR engineered to also be *Stk11/Lkb1* deficient with decreased AMPK alpha activation (Figure S1A). KP and KPL cells form syngeneic tumors with adenocarcinoma histology in C57BL/6J mice (Figure S1B). Subcutaneous KP tumors grew faster than KPL tumors in immunodeficient NSG-SGM3 mice, while KPL grew faster than KP when injected into immune intact C57BL/6J mice (Figures S1C and S1D). Importantly, when KP and KPL cells were injected into *Rag1-deficient* mice (Rag1 KO), the resulting tumors exhibited similar growth patterns (Figure S1E), suggesting that tumor progression differences caused by loss of *Stk1/Lkb1* are mediated by the host adaptive immune system.

Consistent with previous reports in *KL*-mutated NSCLC human tumors, we found that mouse KPL tumors exhibited poor response to anti-PD-1 therapy and a T cell infiltration pattern similar to clinical *STK11/LKB1* mutant individuals reported previously (Figures 1A and S1F).[11] To assess the effect of *Stk11/Lkb1* mutation on the immune landscape of NSCLC, we performed single-cell RNA sequencing (scRNA-seq) on myeloid cells and T cells isolated from KP and KPL syngeneic murine tumors as described.[31] Well-defined cell clusters were annotated with previous reported functional markers (Figures S2A–S2D). CD8 T cells from KP and KPL tumors were aggregated and clustered (see STAR Methods) into terminal exhausted T cells, central memory T cells, proliferating T cells and inhibitory T cells (Figures 1B and S2E).[32,33] The percentage of CD8 T cells from KP and KPL tumors in each cluster demonstrates that loss of *Stk11/Lkb1* expression in tumor cells is associated with a more suppressive CD8 T cell composition in the TME (Figure 1C). Notably, KPL tumors, in contrast to KP tumors, showed a decreased abundance of *Tcf7* expressing CD8 T cells in the KPL TME (Figure 1D). These scRNA-seq observations were confirmed by comparing TCF1$^+$PD-1$^+$CD8 T cells in KP and KPL tumors through flow cytometry and immunohistochemistry (Figures 1E, 1F, S3A, and S3B).

We also evaluated central memory-like CD8 T cell infiltration status in LUAD-affected individuals. First, immunohistochemical analysis of 62 of our NSCLC human tumors showed that *STK11/LKB1* mutant tumors exhibited reduced CD8$^+$, Granzyme B$^+$ (GzB$^+$), or CD45RO$^+$ cells compared with *STK11/LKB1* WT tumors (Figure 1G). Second, we examined The Cancer Genome Atlas (TCGA) database using TIMER deconvolution.[34] In this dataset, *TCF7* expression positively correlated with CD8 T cell infiltration (correlation = 0.31, p = 2.43e-12), and CD8 T cell infiltration was reduced significantly in individuals whose tumors harbor a mutation in *STK11* (Figure 1H). As TCF1-expressing CD8 T cells exhibit central memory features, lack of these cells in our own and TCGA datasets, indicates the lack of tumor-associated memory T cells in the TME of *STK11/LKB1* mutant NSCLC. Collectively, these results suggest the lack of TCF1$^+$CD8 T cells in the TME in *STK11/LKB1* mutant NSCLC, which could impact response to anti-PD-1/PD-L1 treatment.

Bemcentinib-mediated Axl inhibition sensitizes *STK11/LKB1* mutant tumors to anti-PD-1 therapy

Several studies have implicated that Axl expression by tumor or stromal cells participates in anti-tumor immune response and the TME.[23,35–39] To investigate whether systemic inhibition of Axl might sensitize *KL*-mutated tumors to anti-PD-1 treatment, we treated C57BL/6J mice bearing KPL tumors with the selective Axl kinase inhibitor bemcentinib (BGB324) alone, anti-PD-1 alone, or with a combination of anti-PD-1 + BGB324. Although neither treatment alone controlled tumor growth, the combination of BGB324 with anti-PD-1 showed sustained control of tumor progression (Figure 2A). Importantly, BGB324 + anti-PD-1 treatment failed to control the growth of KPL tumors implanted in Rag1 KO mice, demonstrating the therapeutic effect of the

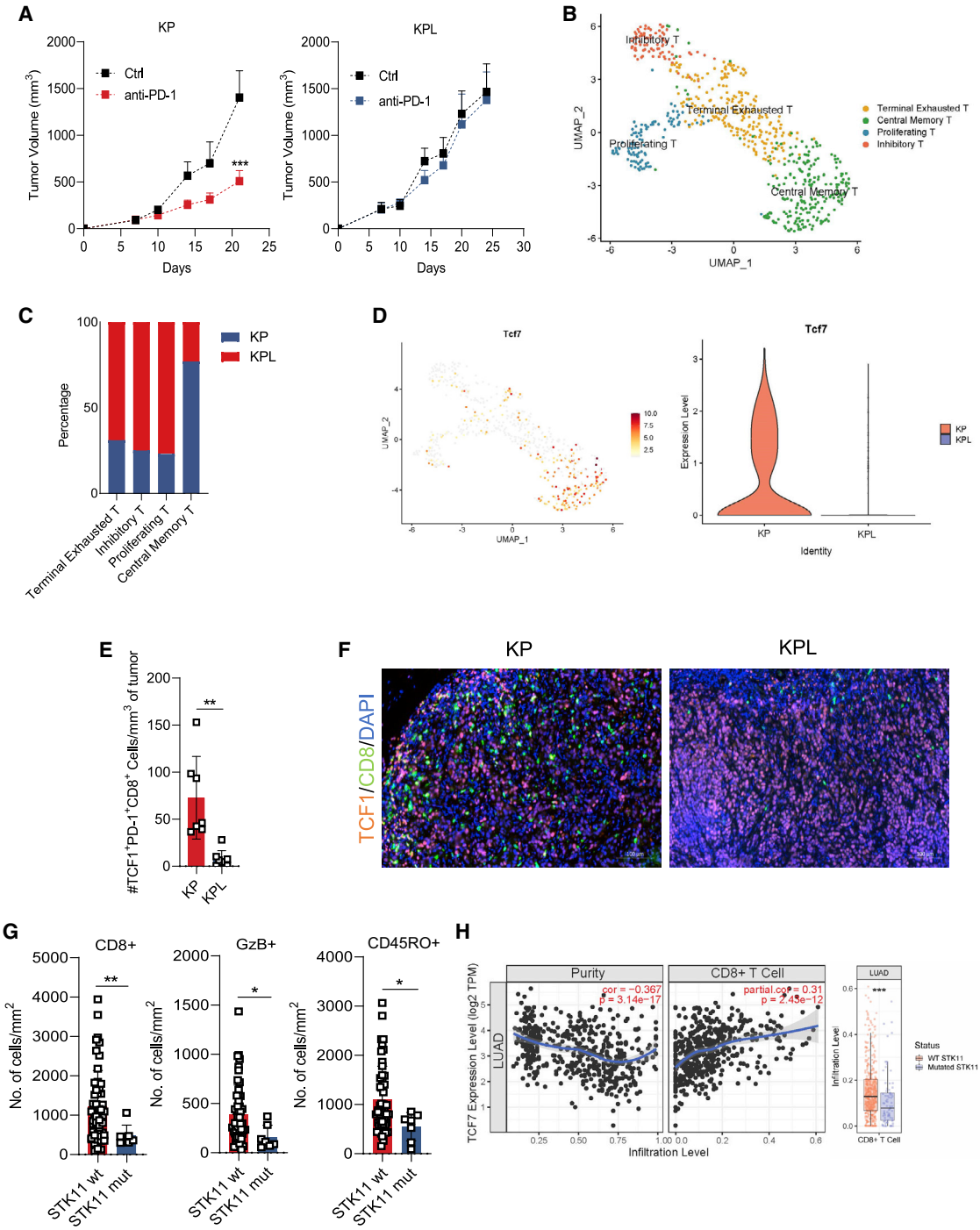

Figure 1. *Stk11/Lkb1* mutant NSCLC lacks anti-PD-1-responsive T cells

(A) C57BL/6J mice (n = 5) were injected with 1 × 10^6 KP (left) or KPL (right) tumor cells and treated with anti-PD-1 (10 mg/kg, day 7, 10, 14). Tumor volume was measured every 3 days. ***p < 0.005.

(B) UMAP of sub-clustering tumor-infiltrating CD8 T cells in KP and KPL tumors. T cell clusters are denoted by color.

(C) Composition of CD8 T cells in each cluster from KP and KPL.

(D) The expression level of *Tcf7* in CD8 T cells of KP and KPL detected from scRNA-seq are compared and visualized through feature plot (left) and violin plot (right).

(E) Abundance of TCF1$^+$PD-1$^+$ cells among gated CD8 tumor-infiltrating lymphocytes (TILs) (per mm^3 of tumor) on day 14 post tumor cell injection. **p < 0.01.

(F) Visualization and localization of TCF1$^+$ (orange) expressing CD8$^+$ (green) T cells in KP (left) and KPL (right) tumor microenvironment through immunohistochemistry. Scale bar, 100 μm.

(legend continued on next page)

combination is dependent on the adaptive immune system (Figure S4A). By deleting CD4 and CD8 T cells respectively *in vivo*, we found that the therapeutic efficacy of combination therapy relies on CD8 T cells but not CD4 T cells (Figures S4B and S4C). To assess the TME from each treatment group, we performed flow cytometry with tumors harvested from C57BL/6J mice. BGB324 treatment alone or in combination with anti-PD-1 increased the infiltration of TCF1$^+$PD-1$^+$CD8 T cells significantly (Figures 2B and S4D). We confirmed that the increased infiltration of TCF1$^+$PD-1$^+$CD8 T cells relies on recruitment from spleen instead of pre-infiltrated T cells, and blocking T cell egress abrogated therapeutic efficacy (Figure S4E). We also treated KP tumors with the same treatment regimen and found that combination therapy was not more effective than anti-PD-1 single-agent therapy and did not alter TCF1$^+$PD-1$^+$CD8 T cell tumor infiltration (Figures S4F–S4G).

To dissect the dynamic changes in the KPL TME after treatment, scRNA-seq with paired single-cell TCR sequencing was performed for four pooled samples of the tumor and its TME from each treatment group and annotated with representative markers (Figures S4A–S4D). Sub-clustering of CD8 T cells revealed eight defined sub-populations based on mRNA expression criteria from previous reports (Figures S4A and S4B).[32,40] Treatment-enriched cells in each cluster within the same treatment group were calculated and compared based on the number of cells observed divided by expected number of cells in each cluster, respectively (Figures 2C and S6C). Treatment of tumors with BGB324 alone significantly enriched CD8 T cells expressing unique TCRs (representing clonally expanded CD8 T cells), with the stem-like T cells and exhausted effector T cells also enriched. Combination therapy showed a trend of enrichment of clonally expanded and exhausted effector CD8 T cells in the TME. TCR lineage tracing to calculate shared TCR clone types between different clusters was performed as described by Guo et al.[32] This analysis demonstrated that the presence of stem-like T cells correlated the most with clonally expanded T cells, which transit into proliferating and exhausted effector T cells capable of performing direct tumor cell killing (Figures 2D, S6D, and S6E). RNA velocity analysis was performed (see STAR Methods) to predict the future transition status of CD8 T cells in the TME. While BGB324 reversed the inhibitory trend observed in control treatment groups and enhanced the stemness of clonally expanded cells, the combination treatment induced clonally expanded T cells into an activated state (Figure 2E).

We then exploited the use of KPL tumor allografts which we engineered to express ova-albumin peptide (KPL-OVA) to allow us to track OVA antigen-specific T cells in their TME. By staining dissociated OVA-expressing tumors with H-2Kb OVA MHC tetramer (SIINFEKL), we found that Axl inhibition with BGB324 increased the number of OVA antigen-specific CD8 T cells in the TME, and in combination with anti-PD-1 further facilitated T cell infiltration (Figures 2F and S7A). However, BGB324 treatment alone did not activate CD8 T cells directly. A combination of BGB324 with anti-PD-1 was required to transit T cells into effector cells which are capable of mediating tumor cell killing (Figures 2G and S7B).

To further validate the role of TCF1$^+$PD-1$^+$CD8 T cells in sensitizing KPL tumors to anti-PD-1 therapy, we treated *Cd8a*^{Cre} or *Cd8a*^{WT} *Tcf7*$^{fl/fl}$ tumor-bearing littermates with combination therapy and found that genetic loss of TCF1 in CD8 cells abolishes therapeutic efficacy (Figure 2H).

These data suggest that pharmacologic inhibition of Axl increases antigen-specific TCF1$^+$PD-1$^+$CD8 T cells in KPL tumors and the expansion of TCF1$^+$PD-1$^+$CD8 T cells are the key population to sensitize KPL tumors to anti-PD-1 therapy.

Inhibition of Axl in dendritic cells is required for efficacy of anti-PD-1 in *STK11/LKB1* mutant tumors

Since Axl inhibition combined with anti-PD-1 controlled KPL tumor growth and this effect was dependent on immune activation, we used *Axl*-deficient mice to investigate whether loss of Axl in host cells is sufficient to sensitize KPL tumors to anti-PD-1 treatment, independent from Axl inhibition-mediated tumor cell killing effect (Figures S8B–S8G). Treatment with anti-PD-1 alone was sufficient to control the growth of KPL tumors grown in *Axl*-deficient mice (Figure 3A). Analysis of the immune landscape of these tumors demonstrated that the loss of Axl in host cells resulted in significantly increased tumor infiltration by TCF1$^+$PD-1$^+$CD8 T cells compared with tumors implanted into *Axl* WT mice (Figures 3B and S8). Therefore, Axl expression in host cells is critical for the suppression of the expansion of TCF1$^+$PD-1$^+$CD8 T cells in the *Stk11/Lkb1* mutant TME.

Through scRNA-seq analysis, we found that *Axl* was expressed in tumor-associated macrophages and dendritic cells (DCs) and was elevated in tumors that lack *Stk11/Lkb1* expression (Figures 3C–3E, S9A, and S9B). To determine which host cell component was critical for Axl inhibition and the therapeutic response to anti-PD-1, macrophages or DCs, were depleted *in vivo*, respectively, as described.[41] Depletion of macrophages did not impact the therapeutic effect of combined Axl and PD-1 inhibition, suggesting that BGB324-mediated sensitization to anti-PD-1 is independent of macrophages (Figure 3F). By contrast, KPL tumors grown in *Batf3*-deficient mice, which lack functional CD103$^+$ DCs that are essential for cross-priming,[42,43] did not respond to combined inhibition of Axl and anti-PD-1 (Figure 3G). These results indicate that inhibiting Axl in DCs is essential for the efficacy of combined Axl and PD-1 inhibition.

Bemcentinib mediated Axl inhibition induced type I interferon secretion expands TCF1$^+$PD-1$^+$CD8$^+$ T cells

As inhibition of Axl in DCs is sufficient to sensitize KPL tumors to anti-PD-1 treatment, we then investigated whether TCF1$^+$PD-1$^+$CD8 T cells are regulated by the Axl-IFNAR pathway.[23,44]

(G) Quantification of immunohistochemistry staining of CD8, Granzyme B (GzB), and CD45RO in *STK11/LKB1* wild-type and mutant individuals. *$p < 0.05$; **$p < 0.01$.

(H) Correlation of *TCF7* expression, tumor purity and CD8 T cell infiltration in TCGA lung adenocarcinoma-affected individuals (left). The expression of *TCF7* negatively correlates with tumor purity, suggesting that the main source of *TCF7* expression detected is stromal and immune cells (correlation = −0.367, p = 3.14e-17). The correlation of CD8 T cell infiltration and *STK11* mutation in lung adenocarcinoma individualss modified from TIMER deconvolution (right).

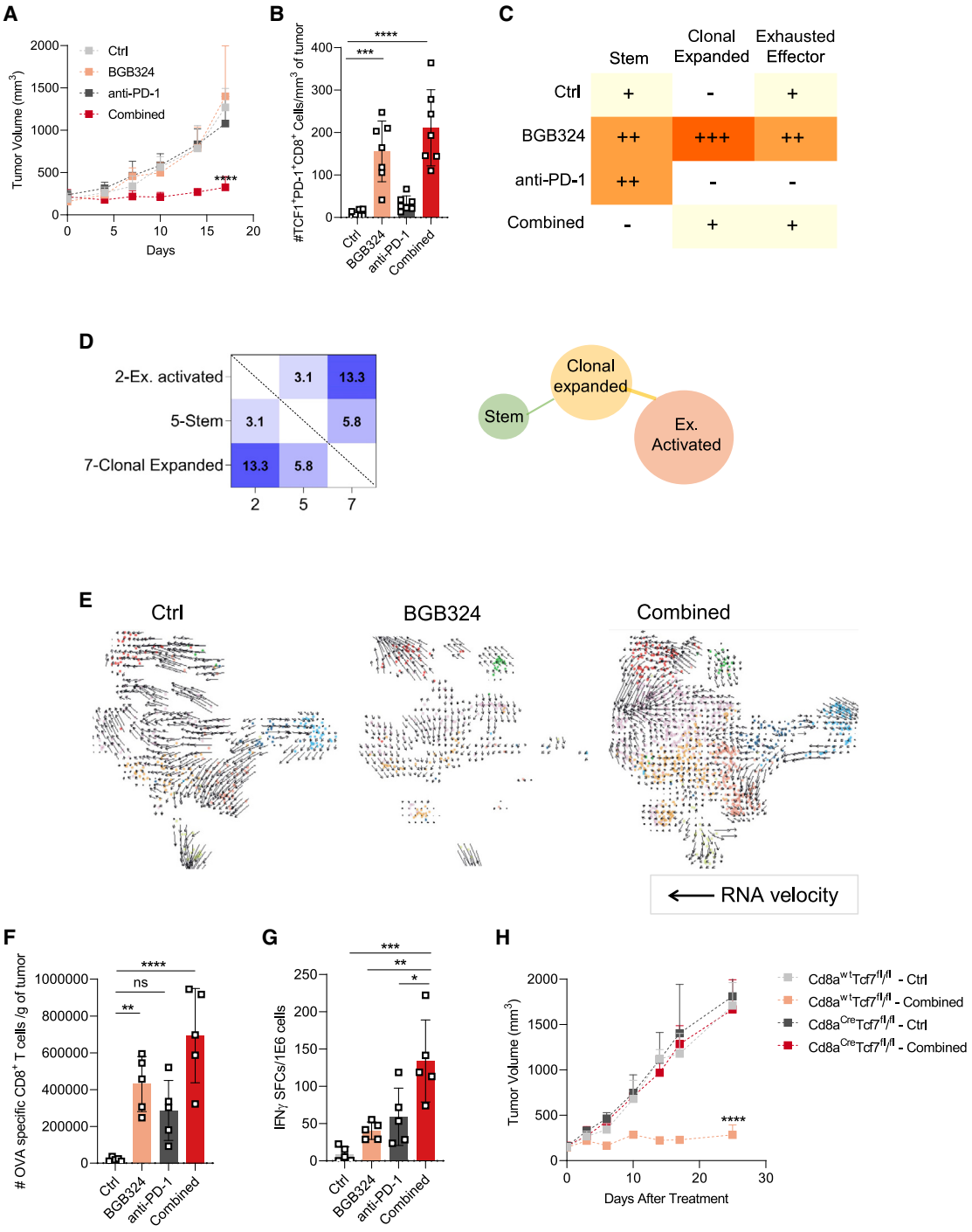

Figure 2. Bemcentinib (BGB324) sensitizes KPL tumors to anti-PD-1

(A) C57BL/6J mice (n = 5) were injected with 1 × 10^6 KPL tumor cells and treated with BGB324 (50 mg/kg, twice daily), anti-PD-1 (10 mg/kg, day 7, 10, 14), or the combination starting on day 7 post tumor cell injection. Control animals were treated with control IgG (10 mg/kg) and vehicle. Tumor volume was measured every 3 days. ****$p < 0.001$.

(B) Abundance of $TCF1^+PD\text{-}1^+$ cells among gated $CD8^+$ T cells (per mm^3 of tumor) on day 7 post therapy initiation (day 14 post tumor cell injection). ***$p < 0.005$; ****$p < 0.001$.

(C) Treatment enriched distribution of stem, clonal expanded, and exhausted effector $CD8^+$ T cells (see STAR Methods). The ratio of observed cell numbers to random expectation estimated by the $R_{o/e}$ index through the chi-square test. +++ ($R_{o/e} \geq 3$, $p < 0.05$) represents highly enriched, ++ ($1.2 \leq R_{o/e} < 3$, $p < 0.05$) represents enriched, + ($0.8 \leq R_{o/e} < 1.2$, $p < 0.05$) represents weakly enriched, − ($0 < R_{o/e} < 0.8$, $p < 0.05$) represents not significant or reduced.

(legend continued on next page)

Bone marrow-derived dendritic cells (BMDCs) were co-cultured with dying KPL tumor cells and treated with BGB324 or DMSO.[45] BMDCs treated with BGB324 showed increased secretion of IFN-β (Figure 4A), which was not observed from BMDCs treated with BGB324 and co-cultured with dying KP cells (data not shown). Increased secretion of IFN-β was also observed through co-culturing *Axl*-deficient BMDCs with dying tumor cells, as well as in tumor lysates from tumors treated with BGB324 (Figures S10A and S10B).

To determine the contribution of type I interferon secretion to BGB324 sensitization of KPL tumors to anti-PD-1 treatment, we inhibited the IFN-αR pharmacologically. Blocking IFN-αR intratumorally diminished response to combined Axl and PD-1 inhibition (Figure 4B) and reduced the infiltration of TCF1$^+$PD-1$^+$CD8 T cells in the TME (Figures 4C, S10C, and S10D). In addition, blocking the IFN-αR counteracted BGB324 induced TCF1 expression on CD8 T cells in co-cultures of BMDCs with OT-1 CD8 T cells stimulated by OVA (see STAR Methods). This suggests that increased TCF1 expression on CD8 T cells by BGB324 treatment is dependent on the type I interferon-IFN-αR axis (Figures 4D and S10E). These results were recapitulated using *Axl* KO BMDCs (Figures 4E and S10F). Furthermore, type I interferon receptor *knockout* T cells adoptively transferred to *Rag*1-deficient mice were unable to respond to BGB324 + anti-PD-1 treatment, while WT T cells adoptively transferred into mice were able to control KPL tumor progression (Figures 4F and S10G). When DCs were stimulated with recombinant IFN-α and co-cultured with CD8 T cells, an increase of TCF1 expression on CD8 T cell was observed both *in vitro* and *in vivo* (Figures S11A–S11D). Taken together, these results demonstrate that increased type I IFN secretion as a result of Axl inhibition is critical for inducing TCF1$^+$PD-1$^+$CD8 T cell expansion in KPL tumors and overcoming resistance to anti-PD-1 therapy.

Bemcentinib sensitizes human *STK11/LKB1* mutant NSCLC to pembrolizumab in a humanized mouse model

To investigate whether the therapeutic effects of combined AXL and PD-1 inhibition apply to human *KL* mutant NSCLCs, we studied two human LUAD *KL*-mutated cell lines, A549 and H2122, in a humanized NSG-SGM3 mouse model. Although these cell lines harbor *KRAS* and *STK11/LKB1* mutations (Figure S12A), A549 express AXL while H2122 has limited AXL expression (Figure 5A). However, the *in vitro* IC_{50} values of BGB324 for growth inhibition of A549 and H2122 tumor cells were similar (Figure 5B). When grown in humanized mice, both xenograft models displayed human AXL expression (Figure 5C). Importantly, BGB324 sensitized A549 and H2122 tumors in humanized mice to pembrolizumab following the schema similar to the effect seen in mouse KPL syngeneic tumors in C57BL/6J mice (Figures 5D–5F and S12B–S12H). In addition, combination therapy resulted in a significant induction of human TCF1$^+$PD-1$^+$CD8$^+$ T cells in each *STK11/LKB1* mutant model (Figures 5G–5H). In summary, BGB324 sensitizes individual-derived *STK11/LKB1* mutant NSCLCs to anti-PD-1 treatment.

Bemcentinib and pembrolizumab combination therapy in *STK11/LKB1* mutant NSCLC-affected individuals

As a part of a multi-arm, ongoing phase II clinical trial of bemcentinib and the anti-PD-1 inhibitor pembrolizumab in previously treated NSCLC (BerGenBio ASA and Merck, Kenilworth NJ, USA, NCT03184571), all individuals with sufficiently large tumor biopsies were subjected to whole-exome sequencing and IHC staining for AXL and PD-L1 expression.[46] Of the 24 chemo-refractory and 30 PD-1 axis inhibitor-refractory individuals sequenced and evaluable for efficacy, three individuals were identified as harboring an *STK11/LKB1* mutation. All three of these individuals experienced clinical benefit from the combination therapy and are presented here as case studies for the efficacy of combined AXL and PD-1 inhibition in *STK11/LKB1* mutant NSCLC.

The first *STK11/LKB1* mutant NSCLC-affected individual is a 79-year-old male who initially achieved a partial response to carboplatin and paclitaxel first-line therapy for 22 months before developing progression of lung and adrenal metastases as well as bone marrow metastasis and enrolling in the study. The individual's tumor biopsy was negative for PD-L1 expression but showed AXL expression in tumor and immune cells (Figures 6A and 6B). The individual went on to achieve a partial response to the bemcentinib/pembrolizumab combination lasting over 10 months from the start of treatment with a maximum target lesion shrinkage of ~50%, after which the individual demonstrated tumor progression and went off study treatment. At the most-recent follow-up date, the individual was still alive and has survived for over 2 years since starting treatment.

The second *STK11/LKB1* mutant NSCLC individual, a 73-year-old male, was treated with first-line pemetrexed and cisplatin and progressed after 8 months. He went onto pembrolizumab monotherapy, where he experienced clinical benefit for 18 months before developing tumor progression with lymph node and chest wall metastases. At the time of screening, the individual's tumor biopsy was PD-L1 weak positive and showed strong expression of AXL in tumor-infiltrating immune cells (Figures 6A and 6C). The individual experienced clinical benefit from the bemcentinib/pembrolizumab drug combination, achieving

(D) Shared clonotypes of TCR between clusters of *Cd8* T cells detected by single-cell TCR sequencing (left). Visualization of heatmap into a network plot is shown (right). See STAR Methods.
(E) RNA velocity analysis of gene expression in *Cd8* T cells from different treatment groups. Arrows indicate potential dynamic paths of differentiation.
(F) C57BL/6J mice (n = 5) were injected with 1 × 10^6 KPL-OVA tumor cells and treated with BGB324 (50 mg/kg, twice daily), anti-PD-1 (10 mg/kg, day 7, 10, 14), or the combination starting on day 7 post tumor cell injection. Control animals were treated with control IgG (10 mg/kg) and vehicle. Abundance of OVA antigen-specific cells among CD8$^+$ T cells (per gram of tumor) in each treatment group analyzed on day 14 after tumor cell injection. **p < 0.01; ****p < 0.001
(G) Same experimental schema as in (F). Statistical results for IFN-γ-producing cells (per mm^3 of tumor) from each treatment group. Splenocytes were isolated and re-stimulated with E7 peptide (negative control) or OVA peptide for 48 h. *p < 0.05; **p < 0.01; ***p < 0.005.
(H) C57BL/6J background conditional knockout mice (n = 5) or control littermates (n = 3 in control, n = 4 in combination treatment) were injected with 1 × 10^6 KPL tumor cells and treated with BGB324 (50 mg/kg, twice daily), anti-PD-1 (10 mg/kg, day 7, 10, 14), or the combination starting on day 7 post tumor cell injection. Control animals were treated with control IgG (10 mg/kg) and vehicle. Tumor volume was measured every 3 days. ****p < 0.001.

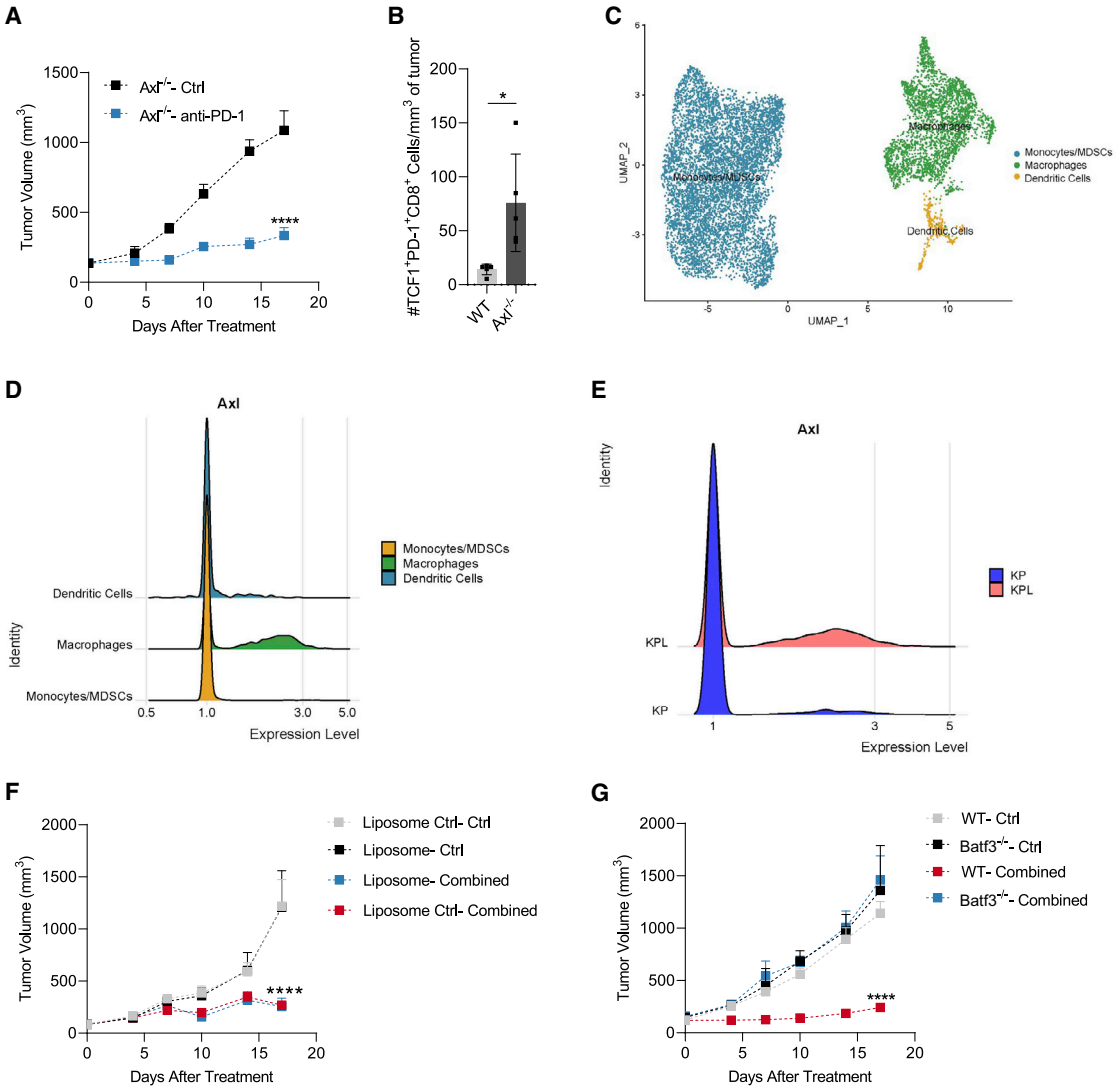

Figure 3. Inhibition of Axl on dendritic cells sensitizes KPL tumors to PD-1 blockade

(A) *Axl*$^{-/-}$ mice (n = 5) were injected with 1 × 10^6 KPL tumor cells and treated with anti-PD-1 (10 mg/kg, days 7, 10, 14). Tumor volume was measured every 3 days. ****p < 0.001.

(B) Abundance of TCF1$^+$PD-1$^+$ cells among gated CD8$^+$ T cells (per mm^3 of tumor) on day 7 post therapy initiation (day 14 post tumor injection). *p < 0.05.

(C) UMAP of sub-clustered tumor-infiltrating myeloid cells in KPL tumors.

(D) Ridge plot of *Axl* expression on myeloid cells in KPL tumor myeloid cell clusters.

(E) Ridge plot of *Axl* expression on myeloid cells in KP and KPL tumors.

(F) C57BL/6J mice (n = 5) were injected with 1 × 10^6 KPL tumor cells and treated with macrophage depleting reagent (Liposome) or control liposomes (Ctrl) (see STAR Methods). Mice were treated with BGB324 (50 mg/kg, twice daily) and anti-PD-1 (10 mg/kg, day 7, 10, 14) (Combined), or corresponding IgG and vehicle (Veh) starting on day 7 post tumor cell injection. Tumor volume was measured every 3 days. ****p < 0.001.

(G) C57BL/6J mice (n = 5) and *Batf3*$^{-/-}$ mice (n = 4 for control group; n = 5 for treatment group) were injected with 1 × 10^6 KPL tumor cells. Treatment strategy same as (F). ****p < 0.001.

stable disease for 3.5 months before receiving a CT scan confirming progressive disease and stopping treatment.

The third *STK11/LKB1* mutant NSCLC individual, a 51-year-old male, initially achieved stable disease to single-agent atezolizumab first-line therapy for 4.6 months before developing progression of lung (mediastinal and pleural) and nodal metastases and enrolling in the study. The individual's tumor biopsy was negative for PD-L1 expression and tumor AXL expression but contained sparse AXL+ immune cells (Figures 6A and 6D). The individual experienced clinical benefit from the study drug combination, achieving stable disease for 6.2 months after which the individual developed bone metastases and was taken off the study treatment due to progressive disease.

While these are three anecdotes, we evaluated our tumor tissue microarray consisting of 62 NSCLC-affected individuals annotated for *STK11/LKB1* mutation status (55 WT, 7 mutant)

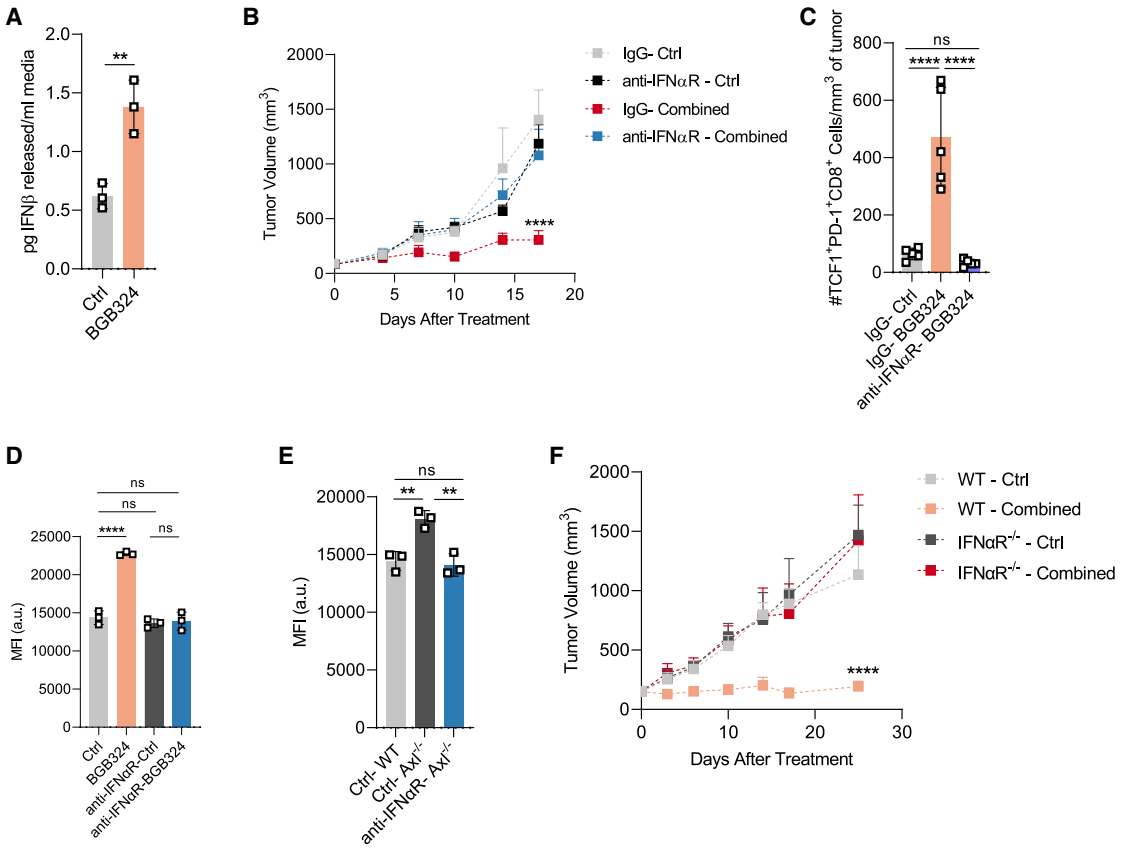

Figure 4. Bemcentinib induced type I interferon secretion is required for TCF1$^+$PD-1$^+$ CD8 cell expansion

(A) BMDCs were co-cultured with irradiated KPL cells (40 Gy) and treated with BGB324 (40 nM) for 24 h. Conditioned medium was collected for IFN-β ELISA. **p < 0.01.

(B) C57BL/6J mice (n = 5) were injected with 1 × 10^6 KPL tumor cells and treated with a control IgG (IgG) or interferon alpha receptor blocking antibody (anti-IFN-αR, see STAR Methods). Mice were treated with BGB324 (50 mg/kg, twice daily) and anti-PD-1 (10 mg/kg, day 7, 10, 14) (combined), or corresponding IgG and vehicle (Ctrl) starting on day 7 post tumor cell injection. Tumor volume was measured every 3 days. ****p < 0.001.

(C) Abundance of TCF1$^+$PD-1$^+$ cells among gated CD8$^+$ T cells (per mm^3 of tumor) at day 7 post therapy initiation. Experimental schema is same as (B). ****p < 0.001.

(D) Mean fluorescent intensity (MFI) for TCF1 in CD8$^+$ OT-1 cells. BMDCs were co-cultured with isolated CD8$^+$ T cells stimulated with ovalbumin (see STAR Methods). Each dot represents one biological replicate. ****p < 0.001.

(E) MFI of TCF1 in CD8$^+$ OT-1 cells. Wild-type BMDCs or *Axl*$^{-/-}$ BMDCs were co-cultured with isolated CD8$^+$ T cells stimulated with ovalbumin for 48h, respectively. IFN-αR blocking strategy is as in (B). **p < 0.01.

(F) *Rag1*$^{-/-}$ mice (n = 5) were transferred with CD8$^+$ T cells isolated from *wild-type* or *Ifnar1*$^{-/-}$ mice. After 7 days of being transferred, mice were injected with 1 × 10^6 KPL tumor cells and treated with BGB324 (50 mg/kg, twice daily) and anti-PD-1 (10 mg/kg, day 7, 10, 14) (combined), or corresponding IgG and vehicle (Ctrl). Tumor volume was measured every 3 days. ****p < 0.001.

for AXL expression. For all the individuals, we find very limited AXL expression in tumor cells. *STK11/LKB1* mutant NSCLC-affected individuals exhibited moderate to strong AXL expression on immune cells, compared with *STK11/LKB1* WT individuals, who displayed more heterogeneous AXL expression (Figure 6E). These results suggest that *STK11/LKB1* mutant NSCLC individuals express AXL in their TME, which has the potential to serve as a biomarker for evaluating combination therapy with bemcentinib and PD-1 inhibitors.

DISCUSSION

In this study, we systematically evaluated response to ICB therapy and the CD8 T cell status in preclinical murine and human models of *KL* mutant NSCLC. We found that mutation of *STK11/LKB1* in tumor cells results in reduced numbers of TCF1$^+$PD-1$^+$CD8 T cells in the TME, which prevents a productive response to anti-PD-1 therapy. We show that inhibition of Axl on DCs in *STK11/LKB1* mutant NSCLC tumors increases TCF1$^+$PD-1$^+$CD8 T cells in the TME and confers sensitivity to PD-1 blockade. Our data also indicate that Axl suppresses DC expression of type I IFNs, which are required for expansion of TCF1$^+$CD8 T cells, thus providing mechanistic insight into the paucity of stem-like T cells in *STK11/LKB1* mutant tumors and a molecular rationale for the poor response of these tumors to PD-1 inhibition. While this study compared *STK11/LKB1* plus *KRAS/TP53* mutant LUADs to LUADs that had only *KRAS/TP53* mutations for the effects of Axl targeting on the TME, it is

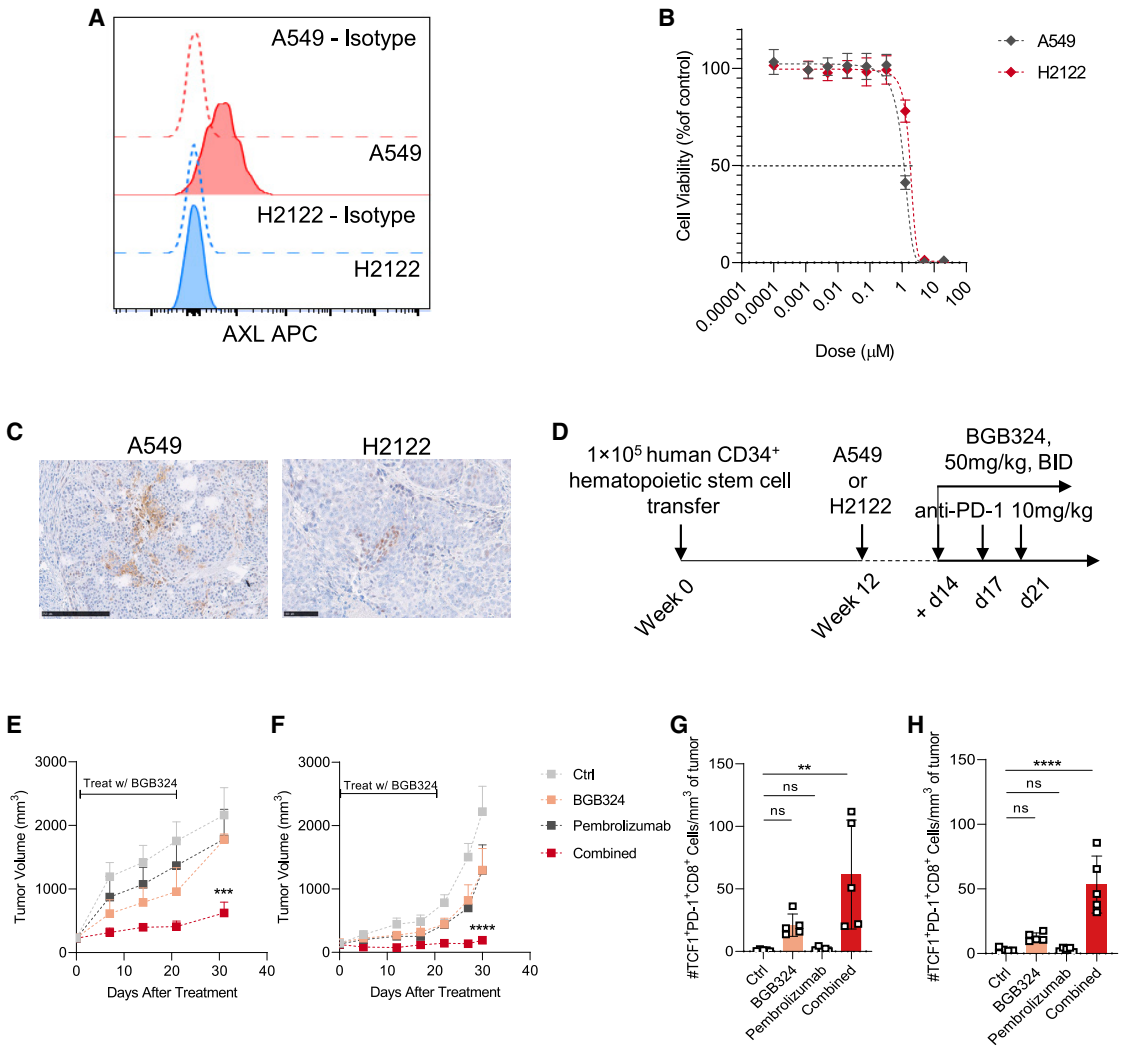

Figure 5. Bemcentinib sensitizes human *STK11/LKB1* mutant NSCLC tumors in humanized mice

(A) Flow cytometric analysis of Axl expression on A549 and H2122 tumor cells *in vitro*. MFI is shown.

(B) The effect of BGB324 on cell viability (IC_{50}) of A549 and H2122 cells.

(C) AXL immunohistochemistry in A549 and H2122 xenografts grown in humanized mice. A549 scale bar, 250 μm; H2122 scale bar, 100 μm.

(D) Humanization and treatment strategy for tumor-bearing humanized mice.

(E) Humanized NSG-SGM3 mice were injected with 1.5×10^6 of A549 cells (n = 5, right flank) and treated with BGB324 (50 mg/kg, twice daily), pembrolizumab (10 mg/kg, day 7, 10, 14), or the combination. Control animals were treated with control IgG (10 mg/kg) and vehicle (Ctrl). Treatment was withdrawn after 20 days. ***$p < 0.005$.

(F) Humanized NSG-SGM3 mice were injected with 1.5×10^6 of H2122 cells (n = 2 for control group and 3 for treatment group, bilateral). Treatment schema is as in (D). Treatment was withdrawn after 20 days. ****$p < 0.001$.

(G and H) Abundance of $TCF1^+PD\text{-}1^+$ cells among gated $CD8^+$ T cells (per mm^3 of tumor) on day 7 post therapy initiation in A549 (G) and H2122 (H) xenografts. **$p < 0.01$; ****$p < 0.001$.

possible that the beneficial effect of Axl inhibition on ICB will extend beyond *STK11/LKB1* mutant NSCLC.

Our scRNA-seq analysis indicates that anti-PD-1 treatment expands all CD8 T cell populations unbiasedly without selective expansion of tumor-associated CD8 T cells specifically. Similar treatment effects of anti-PD-1/PD-L1 were also reported in oral cavity carcinoma models.[47] On the other hand, Axl inhibition induced $TCF1^+PD\text{-}1^+CD8$ T cell expansion, an effect not previously seen with other systemic therapies. Previous studies suggest that $TCF1^+PD\text{-}1^+CD8$ T cells do not secrete IFN-γ or exhibit effector T cell characteristics directly.[20] Thus, while these cells are required for ICB therapy responses, they likely do so by differentiating into effector T cells. Our scRNA-seq analysis with single-cell TCR sequencing lineage tracing suggests that Axl inhibition induces clonal expansion of tumor-specific CD8 T cells from stem cell-like CD8 T cells. However, anti-PD-1 therapy was required for transition into effector T cells ($TCF1^-PD\text{-}1^+CD8$ T cells) and infiltration into tumor cell nests. Although

A

Age/Gender	79 / Male	73 / Male	51 / Male
Previous therapy	Carboplatin / Paclitaxel	Pembrolizumab	Atezolizumab
Previous Therapy PFS	22 months	18 months	4.6 months
STK11 mutation	Moderate LD140PY	Moderate D115V	High S271fs
KRAS mutation	Not detected	Not detected	Not detected
TP53 mutation	High (multiple variants)	Moderate R337L	High R110P
Other relevant mutations	PTEN		KEAP1
PD-L1 TPS	0	15	0
AXL Expression	Tumor and Immune weak pos.	Immune strong pos.	Immune pos.
Target Lesions	1 lung, 1 adrenal	1 lymph node, 1 chest wall	2 lymph node, 1 pleura, 1 lung, 1 mediastinum
Sum Longest Diameter	79 mm	85 mm	129 mm
PFS on study	10.1 months	3.5 months	6.2 months
Overall survival	>33 months (ongoing)	10 months	10 months
Best response	Partial Response	Stable Disease	Stable Disease

[Caption]: Sum of lesion diameters was taken from first CT scan at screening. PFS was calculated as date of first dose to date of confirmatory PD CT scan.

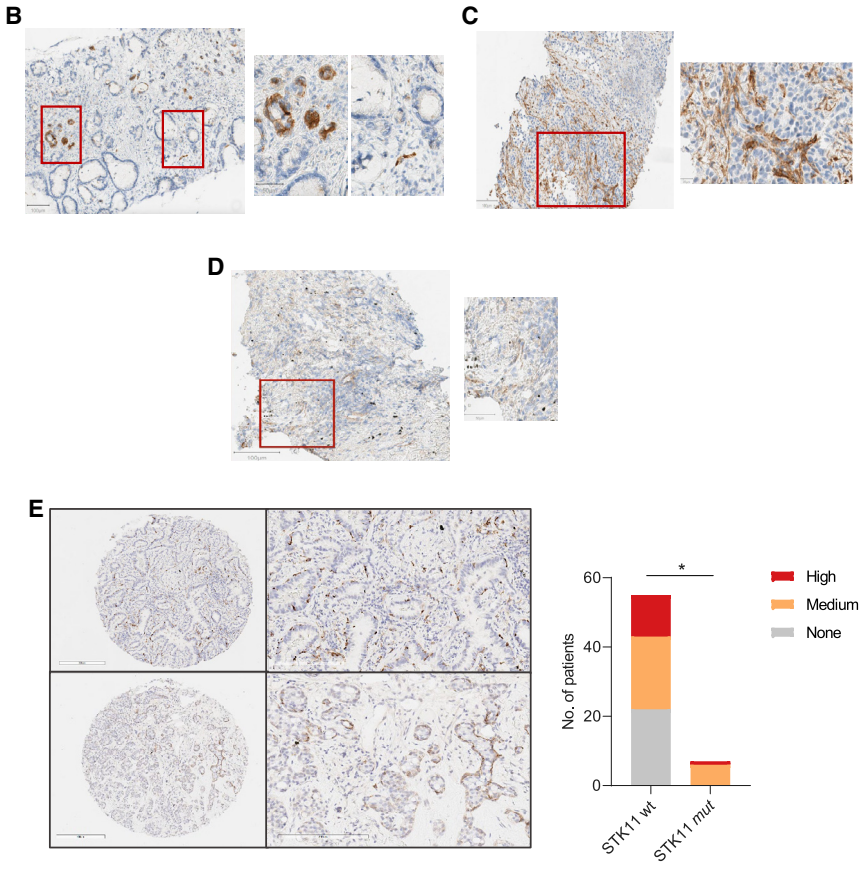

Figure 6. Clinical evidence of the importance of AXL in *STK11/LKB1* mutant NSCLC individualss

(A) *STK11* mutant NSCLC individuals treated with bemcentinib and pembrolizumab combination therapy. All three individuals showed partial response or stable disease, including subjects 2 and 3 who had already progressed on anti-PD-1/PD-L1 therapy.

(B–D) Representative AXL IHC of (B) chemo-refractory individual (scale bar, 100 μm; inset 50 μm) and (C and D) two anti-PD-1/PD-L1 refractory individuals from (A). Magnified regions show examples of AXL^+ tumor (left) and immune (right) cells in (B) and AXL^+ immune cells in (C and D). Scale bar, 100 μm, inset 20 μm in (C); scale bar, 100 μm, inset 50 μm in (D).

(E) Representative AXL IHC staining (left) and the quantification (right) of a tissue microarray consisting of tumors from 62 NSCLC-affected individuals. For the quantification, none represents non-detectable expression of AXL, medium represents 1%–5% percentage of positive staining, and high represents >5% of positive staining. The p value was calculated through chi-square analysis. Scale bar, 300 μm, inset 200 μm. *$p < 0.05$.

Axl is expressed widely on tumor cells, vasculature and myeloid cells,[23,48,49] inhibition of Axl on DCs appears to be the main executor in expanding $TCF1^+PD\text{-}1^+CD8$ T cells to achieve anti-PD-1-mediated control of *STK11/LKB1* mutant NSCLC growth control.

The three NSCLC-affected indviduals treated with bemcentinib and pembrolizumab presented here provide encouraging evidence that inhibiting AXL can re-sensitize human *STK11/LKB1* mutant NSCLC to ICB. This is especially true considering that tumors from these individuals did not harbor KRAS mutations and had minimal to no PD-L1 expression, making them unlikely candidates to respond to anti-PD-1 monotherapy. Although only a small number of STK11-mutant NSCLCs were detected in this trial, the positive responses of these three individuals support the mechanism presented herein.

In conclusion, we have shown in murine- and human-derived preclinical models that systemic treatment with an Axl inhibitor, bemcentinib, in clinical trials combined with PD-1 checkpoint blockade leads to anti-tumor responses in *STK11/LKB1* mutant NSCLCs. Combination treatment is associated with $TCF1^+CD8$ T cell expansion and anti-tumor immune responses. Thus, our data strongly support clinical testing of AXL inhibition in combination with PD-1 checkpoint blockade in *STK11/LKB1* mutant NSCLC individuals and potentially in other tumor settings that are refractory to PD-1 blockade and that also exhibit deficits in $TCF1^+CD8$ T cells. In addition, in these trials it will be important to perform correlative studies that demonstrate, in affected individuals, the effects of AXL inhibition on $TCF1^+CD8$ T cells as well as investigate alternative mechanisms of increasing type I IFN induction to expand tumor-associated $TCF1^+PD\text{-}1^+CD8$ T cells.

Limitations of the study

In this study, we identified that combination of bemcentinib with anti-PD-1 effectively sensitizes *STK11/LKB1* mutant NSCLC tumors in syngeneic models, human-derived xenografts implanted into humanized mice, and anecdotal NSCLC-affected individuals. Mechanistically, bemcentinib increased $TCF1^+CD8$ T cells in the

TME by increasing type I interferon production from DCs. Although we confirmed that the increased abundance of TCF1$^+$CD8 T cells is the key mediator of therapeutic response, our study has limitations. We were unable to study Axl expression at the protein level in tumor-associated immune cells, due to the lack of an available Axl antibody to stain cells isolated from tumor tissues. In addition, more human responses are needed to substantiate the efficacy of the combination treatment in treating STK11/LKB1 mutant NSCLC individuals. In addition, there are reports that *STK11/LKB1* mutant NSCLC individuals have shown response to single-agent PD-1 blockade.[50] Furthermore, it is unclear how specifically the *STK11/LKB1* mutation in these individuals results in a differential response to therapy compared with *STK11/LKB1* WT individuals. At the same time, this treatment regimen may benefit other cancer-affected individuals with different oncogenotypes. We anticipate more clinical evidence will emerge as additional studies are performed.

STAR★METHODS

Detailed methods are provided in the online version of this paper and include the following:

- KEY RESOURCES TABLE
- RESOURCE AVAILABILITY
  - Lead contact
  - Materials availability
  - Data and code availability
- EXPERIMENTAL MODEL AND SUBJECT DETAILS
  - Cell line and reagents
  - Humanized mice and human cord blood sample processing
  - Animal studies
  - Clinical trial
- METHOD DETAILS
  - Cytotoxicity assays
  - OVA expressing cell line generation and characterization
  - *In Vitro* Co-culture of Bone Marrow Dendritic Cells (BMDCs) and T cells
  - Immunoblots
  - Tumor growth and treatment
  - IFN-γ enzyme-linked immunosorbent spot assay (ELISPOT)
  - Enzyme-Linked Immunosorbent Assay (ELISA)
  - Single cell preparation for flow sorting and flow cytometry
  - Library preparation and construction for scRNA-seq and scTCR-seq
  - Flow cytometry analysis
  - Hematoxylin and Eosin (H&E) staining
  - Multiplex immunohistochemistry (IHC)
  - Tissue microarrays immunohistochemistry staining
- QUANTIFICATION AND STATISTICAL ANALYSIS
  - Statistical analysis
  - Flow ytometry cell number normalization
  - scRNA-seq and scTCR-seq data processing
  - Annotation of cell clusters and data visualization
  - Differential expression analysis
  - Characterization of sample enrichment and state transition of T cell clusters
  - RNA velocity analysis
- ADDITIONAL RESOURCES

SUPPLEMENTAL INFORMATION

Supplemental information can be found online at https://doi.org/10.1016/j.xcrm.2022.100554.

ACKNOWLEDGMENTS

This work was supported by a sponsored research agreement from BerGenBio ASA and NIH grants R01 CA243577 and U54 CA210181(to R.A.B.); NIH SPORE P50 CA070907, U54 CA224065, and CPRIT RP160652 (to J.D.M.); RP150072 and RP180725 (to Y.-X.F.); NIH P30 CA142543 (to R.A.B., J.D.M., and Y.-X.F.), the Effie Marie Cain Foundation (to R.A.B.), and CPRIT training grant RP210041(to H.L.). We would like to thank all the individuals who participated in this study. We also thank Zhaoning Wang, Amit Das, Kenneth Huffman, Huocong Huang, Jill Westcott, Long-Shan Li, and Jason Toombs for technical support, instruction, and advice. We thank the technical support of the following laboratory members of the Department of Translational Molecular Pathology Immunoprofiling Laboratory (TMP-IL) at MD Anderson Cancer Center: Mei Jiang, Khaja Khanand, and Jianling Zhou. We also thank the Animal Resources Center, Whole Brain Microscopy Facility, Flow Cytometry Facility, and Tissue Management (P30 CA142543) cores at UT Southwestern for technical assistance and we acknowledge NIH P01 HD087150 for cord blood collection.

AUTHOR CONTRIBUTIONS

Conceptualization, H.L., Z.L., Y.-X.F., J.D.M., and R.A.B.; methodology, H.L., Z.L., H.Z., L.L., L.G., C.D., J.Y., X.L., and B.L.; investigation, H.L., Z.L., C.H., H.Z., L.L., L.G., H.P., A.Z., C.D., J.Y., A.R., D.G., M.P., X.L., K.A., X.C., L.S., C.B., S.H.-R., L.W., and D.M., writing, H.L., A.R., D.M., H.G., J.B.L., J.D.M., and R.A.B.; funding acquisition, Y.-X.F., J.D.M., and R.A.; resources, S.H., E.A.A., I.W., M.C., H.G., G.G., J.B.L., B.L., J.D.M., and J.V.H.; supervision, Y.-X.F., J.D.M., and R.A.B.

DECLARATION OF INTERESTS

This work was supported in part by a sponsored research agreement from BerGenBio ASA to R.A.B. A.R., D.M., H.G., and G.G. are current employees of BerGenBio ASA and J.B.L. is a former employee of BerGenBio ASA. M.C. is a current employee of Merck &Co., Inc., Kenilworth, NJ. J.D.M. receives licensing royalties from the NIH and UTSW for distribution of human tumor lines. H.L., Z.L., D.M., J.B.L., J.D.M., and R.A.B. are authors of a patent related to this study. The remaining authors have no competing interests.

Received: May 10, 2021
Revised: October 22, 2021
Accepted: February 8, 2022
Published: March 15, 2022

REFERENCES

1. Gandhi, L., Rodriguez-Abreu, D., Gadgeel, S., Esteban, E., Felip, E., De Angelis, F., Domine, M., Clingan, P., Hochmair, M.J., Powell, S.F., et al. (2018). Pembrolizumab plus chemotherapy in metastatic non-small-cell lung cancer. N. Engl. J. Med. *378*, 2078–2092.
2. Hellmann, M.D., Ciuleanu, T.E., Pluzanski, A., Lee, J.S., Otterson, G.A., Audigier-Valette, C., Minenza, E., Linardou, H., Burgers, S., Salman, P., et al. (2018). Nivolumab plus ipilimumab in lung cancer with a high tumor mutational burden. N. Engl. J. Med. *378*, 2093–2104.

3. Carbone, D.P., Reck, M., Paz-Ares, L., Creelan, B., Horn, L., Steins, M., Felip, E., van den Heuvel, M.M., Ciuleanu, T.E., Badin, F., et al. (2017). First-line nivolumab in stage IV or recurrent non-small-cell lung cancer. N. Engl. J. Med. *376*, 2415–2426.

4. Garon, E.B., Rizvi, N.A., Hui, R., Leighl, N., Balmanoukian, A.S., Eder, J.P., Patnaik, A., Aggarwal, C., Gubens, M., Horn, L., et al. (2015). Pembrolizumab for the treatment of non-small-cell lung cancer. N. Engl. J. Med. *372*, 2018–2028.

5. Jeanson, A., Tomasini, P., Souquet-Bressand, M., Brandone, N., Boucekine, M., Grangeon, M., Chaleat, S., Khobta, N., Milia, J., Mhanna, L., et al. (2019). Efficacy of immune checkpoint inhibitors in KRAS-mutant non-small cell lung cancer (NSCLC). J. Thorac. Oncol. *14*, 1095–1101.

6. Kim, J.H., Kim, H.S., and Kim, B.J. (2017). Prognostic value of KRAS mutation in advanced non-small-cell lung cancer treated with immune checkpoint inhibitors: a meta-analysis and review. Oncotarget *8*, 48248–48252.

7. Cho, B.C., Lopes, G., Kowalski, D.M., Kasahara, K., Wu, Y.-L., Castro, G., Turna, H.Z., Cristescu, R., Aurora-Garg, D., Loboda, A., et al. (2020). Abstract CT084: relationship between STK11 and KEAP1 mutational status and efficacy in KEYNOTE-042: pembrolizumab monotherapy versus platinum-based chemotherapy as first-line therapy for PD-L1-positive advanced NSCLC. Cancer Res. *80*, CT084.

8. Koivunen, J.P., Kim, J., Lee, J., Rogers, A.M., Park, J.O., Zhao, X., Naoki, K., Okamoto, I., Nakagawa, K., Yeap, B.Y., et al. (2008). Mutations in the LKB1 tumour suppressor are frequently detected in tumours from Caucasian but not Asian lung cancer patients. Br. J. Cancer *99*, 245–252.

9. Shire, N.J., Klein, A.B., Golozar, A., Collins, J.M., Fraeman, K.H., Nordstrom, B.L., McEwen, R., Hembrough, T., and Rizvi, N.A. (2020). STK11 (LKB1) mutations in metastatic NSCLC: prognostic value in the real world. PLoS One *15*, e0238358.

10. Skoulidis, F., Arbour, K.C., Hellmann, M.D., Patil, P.D., Marmarelis, M.E., Awad, M.M., Murray, J.C., Hellyer, J., Gainor, J.F., Dimou, A., et al. (2019). Association of STK11/LKB1 genomic alterations with lack of benefit from the addition of pembrolizumab to platinum doublet chemotherapy in non-squamous non-small cell lung cancer. J. Clin. Oncol. *37*, 102.

11. Skoulidis, F., Goldberg, M.E., Greenawalt, D.M., Hellmann, M.D., Awad, M.M., Gainor, J.F., Schrock, A.B., Hartmaier, R.J., Trabucco, S.E., Gay, L., et al. (2018). STK11/LKB1 mutations and PD-1 inhibitor resistance in KRAS-mutant lung adenocarcinoma. Cancer Discov. *8*, 822–835.

12. Hollstein, P.E., Eichner, L.J., Brun, S.N., Kamireddy, A., Svensson, R.U., Vera, L.I., Ross, D.S., Rymoff, T.J., Hutchins, A., Galvez, H.M., et al. (2019). The AMPK-related kinases SIK1 and SIK3 mediate key tumor-suppressive effects of LKB1 in NSCLC. Cancer Discov. *9*, 1606–1627.

13. Shackelford, D.B., and Shaw, R.J. (2009). The LKB1-AMPK pathway: metabolism and growth control in tumour suppression. Nat. Rev. Cancer *9*, 563–575.

14. Woods, A., Johnstone, S.R., Dickerson, K., Leiper, F.C., Fryer, L.G., Neumann, D., Schlattner, U., Wallimann, T., Carlson, M., and Carling, D. (2003). LKB1 is the upstream kinase in the AMP-activated protein kinase cascade. Curr. Biol. *13*, 2004–2008.

15. Kadara, H., Choi, M., Zhang, J., Parra, E.R., Rodriguez-Canales, J., Gaffney, S.G., Zhao, Z., Behrens, C., Fujimoto, J., Chow, C., et al. (2017). Whole-exome sequencing and immune profiling of early-stage lung adenocarcinoma with fully annotated clinical follow-up. Ann. Oncol. *28*, 75–82.

16. Koyama, S., Akbay, E.A., Li, Y.Y., Aref, A.R., Skoulidis, F., Herter-Sprie, G.S., Buczkowski, K.A., Liu, Y., Awad, M.M., Denning, W.L., et al. (2016). STK11/LKB1 deficiency promotes neutrophil recruitment and proinflammatory cytokine production to suppress T-cell activity in the lung tumor microenvironment. Cancer Res. *76*, 999–1008.

17. Chen, Z., Ji, Z., Ngiow, S.F., Manne, S., Cai, Z., Huang, A.C., Johnson, J., Staupe, R.P., Bengsch, B., Xu, C., et al. (2019). TCF-1-Centered transcriptional network drives an effector versus exhausted CD8 T cell-fate decision. Immunity *51*, 840–855 e845.

18. Im, S.J., Hashimoto, M., Gerner, M.Y., Lee, J., Kissick, H.T., Burger, M.C., Shan, Q., Hale, J.S., Lee, J., Nasti, T.H., et al. (2016). Defining CD8+ T cells that provide the proliferative burst after PD-1 therapy. Nature *537*, 417–421.

19. Miller, B.C., Sen, D.R., Al Abosy, R., Bi, K., Virkud, Y.V., LaFleur, M.W., Yates, K.B., Lako, A., Felt, K., Naik, G.S., et al. (2019). Subsets of exhausted CD8(+) T cells differentially mediate tumor control and respond to checkpoint blockade. Nat. Immunol. *20*, 326–336.

20. Siddiqui, I., Schaeuble, K., Chennupati, V., Fuertes Marraco, S.A., Calderon-Copete, S., Pais Ferreira, D., Carmona, S.J., Scarpellino, L., Gfeller, D., Pradervand, S., et al. (2019). Intratumoral Tcf1(+)PD-1(+)CD8(+) T cells with stem-like properties promote tumor control in response to vaccination and checkpoint blockade immunotherapy. Immunity *50*. 195–211. e110.

21. Utzschneider, D.T., Charmoy, M., Chennupati, V., Pousse, L., Ferreira, D.P., Calderon-Copete, S., Danilo, M., Alfei, F., Hofmann, M., Wieland, D., et al. (2016). T cell factor 1-expressing memory-like CD8(+) T cells sustain the immune response to chronic viral infections. Immunity *45*, 415–427.

22. Ludwig, K.F., Du, W., Sorrelle, N.B., Wnuk-Lipinska, K., Topalovski, M., Toombs, J.E., Cruz, V.H., Yabuuchi, S., Rajeshkumar, N.V., Maitra, A., et al. (2018). Small-molecule inhibition of Axl targets tumor immune suppression and enhances chemotherapy in pancreatic cancer. Cancer Res. *78*, 246–255.

23. Rothlin, C.V., Ghosh, S., Zuniga, E.I., Oldstone, M.B., and Lemke, G. (2007). TAM receptors are pleiotropic inhibitors of the innate immune response. Cell *131*, 1124–1136.

24. Varnum, B.C., Young, C., Elliott, G., Garcia, A., Bartley, T.D., Fridell, Y.W., Hunt, R.W., Trail, G., Clogston, C., Toso, R.J., et al. (1995). Axl receptor tyrosine kinase stimulated by the vitamin K-dependent protein encoded by growth-arrest-specific gene 6. Nature *373*, 623–626.

25. Chen, J., Yang, Y.F., Yang, Y., Zou, P., Chen, J., He, Y., Shui, S.L., Cui, Y.R., Bai, R., Liang, Y.J., et al. (2018). AXL promotes Zika virus infection in astrocytes by antagonizing type I interferon signalling. Nat. Microbiol. *3*, 302–309.

26. Diamond, M.S., Kinder, M., Matsushita, H., Mashayekhi, M., Dunn, G.P., Archambault, J.M., Lee, H., Arthur, C.D., White, J.M., Kalinke, U., et al. (2011). Type I interferon is selectively required by dendritic cells for immune rejection of tumors. J. Exp. Med. *208*, 1989–2003.

27. Fuertes, M.B., Woo, S.R., Burnett, B., Fu, Y.X., and Gajewski, T.F. (2013). Type I interferon response and innate immune sensing of cancer. Trends Immunol. *34*, 67–73.

28. Scutera, S., Fraone, T., Musso, T., Cappello, P., Rossi, S., Pierobon, D., Orinska, Z., Paus, R., Bulfone-Paus, S., and Giovarelli, M. (2009). Survival and migration of human dendritic cells are regulated by an IFN-alpha-inducible Axl/Gas6 pathway. J. Immunol. *183*, 3004–3013.

29. Seitz, H.M., Camenisch, T.D., Lemke, G., Earp, H.S., and Matsushima, G.K. (2007). Macrophages and dendritic cells use different Axl/Mertk/Tyro3 receptors in clearance of apoptotic cells. J. Immunol. *178*, 5635–5642.

30. Guo, Z., Li, Y., Zhang, D., and Ma, J. (2017). Axl inhibition induces the antitumor immune response which can be further potentiated by PD-1 blockade in the mouse cancer models. Oncotarget *8*, 89761–89774.

31. Zhou, T., Damsky, W., Weizman, O.E., McGeary, M.K., Hartmann, K.P., Rosen, C.E., Fischer, S., Jackson, R., Flavell, R.A., Wang, J., et al. (2020). IL-18BP is a secreted immune checkpoint and barrier to IL-18 immunotherapy. Nature *583*, 609–614.

32. Guo, X., Zhang, Y., Zheng, L., Zheng, C., Song, J., Zhang, Q., Kang, B., Liu, Z., Jin, L., Xing, R., et al. (2018). Global characterization of T cells in non-small-cell lung cancer by single-cell sequencing. Nat. Med. *24*, 978–985.

33. Luoma, A.M., Suo, S., Williams, H.L., Sharova, T., Sullivan, K., Manos, M., Bowling, P., Hodi, F.S., Rahma, O., Sullivan, R.J., et al. (2020). Molecular

pathways of colon inflammation induced by cancer immunotherapy. Cell *182*, 655–671 e622.

34. Li, B., Liu, J.S., and Liu, X.S. (2017). Revisit linear regression-based deconvolution methods for tumor gene expression data. Genome Biol. *18*, 127.
35. Aguilera, T.A., Rafat, M., Castellini, L., Shehade, H., Kariolis, M.S., Hui, A.B., Stehr, H., von Eyben, R., Jiang, D., Ellies, L.G., et al. (2016). Reprogramming the immunological microenvironment through radiation and targeting Axl. Nat. Commun. *7*, 13898.
36. Lotsberg, M.L., Wnuk-Lipinska, K., Terry, S., Tan, T.Z., Lu, N., Trachsel-Moncho, L., Rosland, G.V., Siraji, M.I., Hellesoy, M., Rayford, A., et al. (2020). AXL targeting abrogates autophagic flux and induces immunogenic cell death in drug-resistant cancer cells. J. Thorac. Oncol. *15*, 973–999.
37. Schmid, E.T., Pang, I.K., Carrera Silva, E.A., Bosurgi, L., Miner, J.J., Diamond, M.S., Iwasaki, A., and Rothlin, C.V. (2016). AXL receptor tyrosine kinase is required for T cell priming and antiviral immunity. Elife *5*, e12414.
38. Tsukita, Y., Fujino, N., Miyauchi, E., Saito, R., Fujishima, F., Itakura, K., Kyogoku, Y., Okutomo, K., Yamada, M., Okazaki, T., et al. (2019). Axl kinase drives immune checkpoint and chemokine signalling pathways in lung adenocarcinomas. Mol. Cancer *18*, 24.
39. Zagorska, A., Traves, P.G., Lew, E.D., Dransfield, I., and Lemke, G. (2014). Diversification of TAM receptor tyrosine kinase function. Nat. Immunol. *15*, 920–928.
40. Yost, K.E., Satpathy, A.T., Wells, D.K., Qi, Y., Wang, C., Kageyama, R., McNamara, K.L., Granja, J.M., Sarin, K.Y., Brown, R.A., et al. (2019). Clonal replacement of tumor-specific T cells following PD-1 blockade. Nat. Med. *25*, 1251–1259.
41. Ren, Z., Guo, J., Liao, J., Luan, Y., Liu, Z., Sun, Z., Liu, X., Liang, Y., Peng, H., and Fu, Y.X. (2017). CTLA-4 limits anti-CD20-mediated tumor regression. Clin. Cancer Res. *23*, 193–203.
42. Broz, M.L., Binnewies, M., Boldajipour, B., Nelson, A.E., Pollack, J.L., Erle, D.J., Barczak, A., Rosenblum, M.D., Daud, A., Barber, D.L., et al. (2014). Dissecting the tumor myeloid compartment reveals rare activating antigen-presenting cells critical for T cell immunity. Cancer Cell *26*, 638–652.
43. Edelson, B.T., Kc, W., Juang, R., Kohyama, M., Benoit, L.A., Klekotka, P.A., Moon, C., Albring, J.C., Ise, W., Michael, D.G., et al. (2010). Peripheral CD103+ dendritic cells form a unified subset developmentally related to CD8alpha+ conventional dendritic cells. J. Exp. Med. *207*, 823–836.
44. Li, W., Lu, L., Lu, J., Wang, X., Yang, C., Jin, J., Wu, L., Hong, X., Li, F., Cao, D., et al. (2020). cGAS-STING-mediated DNA sensing maintains CD8(+) T cell stemness and promotes antitumor T cell therapy. Sci. Transl Med. *12*, eaay9013.
45. Han, C., Liu, Z., Zhang, Y., Shen, A., Dong, C., Zhang, A., Moore, C., Ren, Z., Lu, C., Cao, X., et al. (2020). Tumor cells suppress radiation-induced immunity by hijacking caspase 9 signaling. Nat. Immunol. *21*, 546–554.
46. Felip, E., Brunsvig, P., Vinolas, N., Aix, S.P., Costa, E.C., Gomez, M.D., Perez, J.M.T., Arriola, E., Campelo, R.G., Spicer, J.F., et al. (2019). A phase II study of bemcentinib (BGB324), a first-in-class highly selective AXL inhibitor, with pembrolizumab in pts with advanced NSCLC: OS for stage I and preliminary stage II efficacy. J. Clin. Oncol. *37*, 9098.
47. Friedman, J., Moore, E.C., Zolkind, P., Robbins, Y., Clavijo, P.E., Sun, L., Greene, S., Morisada, M.V., Mydlarz, W.K., Schmitt, N., et al. (2020). Neoadjuvant PD-1 immune checkpoint blockade reverses functional immunodominance among tumor antigen-specific T cells. Clin. Cancer Res. *26*, 679–689.
48. Gay, C.M., Balaji, K., and Byers, L.A. (2017). Giving AXL the axe: targeting AXL in human malignancy. Br. J. Cancer *116*, 415–423.
49. Maier, B., Leader, A.M., Chen, S.T., Tung, N., Chang, C., LeBerichel, J., Chudnovskiy, A., Maskey, S., Walker, L., Finnigan, J.P., et al. (2020). A conserved dendritic-cell regulatory program limits antitumour immunity. Nature *580*, 257–262.
50. Ricciuti, B., Arbour, K.C., Lin, J.J., Vajdi, A., Vokes, N., Hong, L., Zhang, J., Tolstorukov, M.Y., Li, Y.Y., Spurr, L.F., et al. (2021). Diminished efficacy of programmed death-(Ligand)1 inhibition in STK11- and KEAP1-mutant lung adenocarcinoma is affected by KRAS mutation status. J. Thorac. Oncol. https://doi.org/10.1016/j.jtho.2021.10.013.
51. Stuart, T., Butler, A., Hoffman, P., Hafemeister, C., Papalexi, E., Mauck, W.M., 3rd, Hao, Y., Stoeckius, M., Smibert, P., and Satija, R. (2019). Comprehensive integration of single-cell data. Cell *177*, 1888–1902 e1821.
52. Qiu, X., Mao, Q., Tang, Y., Wang, L., Chawla, R., Pliner, H.A., and Trapnell, C. (2017). Reversed graph embedding resolves complex single-cell trajectories. Nat. Methods *14*, 979–982.
53. Trapnell, C., Cacchiarelli, D., Grimsby, J., Pokharel, P., Li, S., Morse, M., Lennon, N.J., Livak, K.J., Mikkelsen, T.S., and Rinn, J.L. (2014). The dynamics and regulators of cell fate decisions are revealed by pseudotemporal ordering of single cells. Nat. Biotechnol. *32*, 381–386.
54. Aran, D., Looney, A.P., Liu, L., Wu, E., Fong, V., Hsu, A., Chak, S., Naikawadi, R.P., Wolters, P.J., Abate, A.R., et al. (2019). Reference-based analysis of lung single-cell sequencing reveals a transitional profibrotic macrophage. Nat. Immunol. *20*, 163–172.
55. Wickham, H. (2016). ggplot2: Elegant Graphics for Data Analysis (Springer International Publishing).
56. La Manno, G., Soldatov, R., Zeisel, A., Braun, E., Hochgerner, H., Petukhov, V., Lidschreiber, K., Kastriti, M.E., Lonnerberg, P., Furlan, A., et al. (2018). RNA velocity of single cells. Nature *560*, 494–498.
57. McInnes, L., and Healy, J. (2018). UMAP: Uniform Manifold Approximation and Projection for Dimension Reduction. Preprint at ArXiv. abs/1802.03426.
58. Mender, I., Zhang, A., Ren, Z., Han, C., Deng, Y., Siteni, S., Li, H., Zhu, J., Vemula, A., Shay, J.W., et al. (2020). Telomere stress potentiates STING-dependent anti-tumor immunity. Cancer Cell *38*, 400–411.e6.
59. Park, C.Y., Majeti, R., and Weissman, I.L. (2008). In vivo evaluation of human hematopoiesis through xenotransplantation of purified hematopoietic stem cells from umbilical cord blood. Nat. Protoc. *3*, 1932–1940.
60. Wunderlich, M., Chou, F.S., Link, K.A., Mizukawa, B., Perry, R.L., Carroll, M., and Mulloy, J.C. (2010). AML xenograft efficiency is significantly improved in NOD/SCID-IL2RG mice constitutively expressing human SCF, GM-CSF and IL-3. Leukemia *24*, 1785–1788.
61. Yang, X., Zhang, X., Fu, M.L., Weichselbaum, R.R., Gajewski, T.F., Guo, Y., and Fu, Y.X. (2014). Targeting the tumor microenvironment with interferon-beta bridges innate and adaptive immune responses. Cancer Cell *25*, 37–48.
62. Sorrelle, N., Ganguly, D., Dominguez, A.T.A., Zhang, Y., Huang, H., Dahal, L.N., Burton, N., Ziemys, A., and Brekken, R.A. (2019). Improved multiplex immunohistochemistry for immune microenvironment evaluation of mouse formalin-fixed, paraffin-embedded tissues. J. Immunol. *202*, 292–299.
63. Becht, E., McInnes, L., Healy, J., Dutertre, C.A., Kwok, I.W.H., Ng, L.G., Ginhoux, F., and Newell, E.W. (2018). Dimensionality reduction for visualizing single-cell data using UMAP. Nat. Biotechnol. https://doi.org/10.1038/nbt.4314.

STAR★METHODS

KEY RESOURCES TABLE

REAGENT or RESOURCE	SOURCE	IDENTIFIER
Antibodies		
InVivoMab anti-mouse PD-1 (RMP1-14)	BioXCell	Cat# BE0146; RRID: AB_10949053
InVivoMab rat IgG2a isotype control (2A3)	BioXCell	Cat# BE0089; RRID: AB_11007769
InVivoMab anti-human PD-1 (J110)	BioXCell	Cat# BE0193; RRID: AB_109850168
InVivoMab mouse IgG1 isotype control (MOPC-21)	BioXCell	Cat# BE0083; RRID: AB_1107784
InVivoMab anti-mouse IFNAR-1 (MAR1-5A3)	BioXCell	Cat# BE0241; RRID: AB_2687723
anti-PD-1 (Pembrolizumab)		N/A
Anti-mCD45 (Flow cytometry, 30-F11)	BioLegend	Cat# 103126; RRID: AB_493535
Anti-mCD3 (Flow cytometry, 145-2C11)	BD Bioscience	Cat# 564379; RRID: AB_2738780
Anti-mCD4 (Flow cytometry, GK1.5)	BioLegend	Cat# 100413; RRID: AB_312698
Anti-mCD8α (Flow cytometry, 53-6.7)	BioLegend	Cat# 100730; RRID: AB_493703
Anti-mCD8b (Flow cytometry, YTS156.7.7)	BioLegend	Cat# 126616; RRID: AB_2562777
Anti-mPD-1 (Flow cytometry, 29F.1A12)	BioLegend	Cat# 135224; RRID: AB_2563523
Anti-mKi-67 (Flow cytometry, 16A8)	BioLegend	Cat# 652404; RRID: AB_2562664
OVA257-264 (SIINFEKL) peptide bound to H-2Kb Monoclonal Antibody (Flow cytometry, 25-D1.16)	eBioscience	Cat# 17-5743-82; RRID: AB_1311286
Anti-h/Mtcf1/7 (Flow cytometry, C63D9)	Cell Signaling Technologies	Cat# 6444; RRID: AB_2797627
Biotin anti-mouse CD45 Antibody (30-F11)	BioLegend	Cat# 101304; RRID: AB_312969
Rabbit (DA1E) mAb IgG XP® Isotype Contorl	Cell Signaling Technologies	Cat# 2975; RRID: AB_10699151
Anti-hCD45 (Flow cytometry, HI30)	BioLegend	Cat# 304021; RRID: AB_493654
Anti-hCD3 (Flow cytometry, HIT3a)	BioLegend	Cat# 300327; RRID: AB_1575010
Fixable Viability Dye eFluor™ 506	Thermo Fisher	Cat# 65-0866-18
iTAg Tetramer/PE – H-2 Kb OVA (SIINFEKL)	MBL	Cat# TB-5001-1
Anti-Fcγiii/ii receptor (clone 2.4G2)	BD Biosciences	CAT# 553141, RRID: AB_394656
TCF1/TCF7 (C63D9) Rabbit mAb	Cell Signaling Technologies	Cat# 2203; RRID: AB_2199302
CD8α (D4W2Z) XP® Rabbit mAb	Cell Signaling Technologies	Cat# 98941; RRID: AB_2756376
LKB1 (D60C5) Rabbit mAb	Cell Signaling Technologies	Cat# 3047; RRID: AB_2198327
AXL (C89E7) Rabbit mAb	Cell Signaling Technologies	Cat# 8661; RRID: AB_11217435
GAPDH (D16H11) Rabbit mAb	Cell Signaling Technologies	Cat# 5174; RRID: AB_10622025
Anti-rabbit IgG, HRP-linked Antibody	Cell Signaling Technologies	Cat# 7074; RRID: AB_2099233
Chemicals, peptides, and recombinant proteins		
TMB Solution (1X)	eBioscience	Cat# 00-4201-56
Sulfadiazine/ Trimethoprim (Aurora Pharmaceutical LLC)	UTSW-Veterinary Drug Services	Cat# 302
GE Healthcare Ficoll-Paque™ Premium	Cytiva	Cat# 17544203
Animal free Collagenase, type A	Sigma	Cat# SCR136
DNAse I	Roche	Cat# 11284932001
Recombinant murine GM-CSF	Peprotech	Cat# 315-03
Recombinant murine IFN-γ	Peprotech	Cat# 210-10
Recombinant human IL-4	Peprotech	Cat# 400-04
Recombinant human GM-CSF	Peprotech	Cat# 300-03
Recombinant human TNFα	Peprotech	Cat# 300-01A
Clophsome®-A-Clodronate Liposomes (Anionic)	FormuMax Scientific	Cat# F70101C-A
$OVA_{257-264}$ (SIINFEKL)	InvivoGen	Cat# vac-sin
Human Ppillomavirus (HPV) E7 protein (49-57)	GenScript	Cat# RP20249

(*Continued on next page*)

Continued

REAGENT or RESOURCE	SOURCE	IDENTIFIER
Ovalbumin	Sigma-Aldrich	Cat# A2512
pCpGfree-OVA	InvivoGen	Cat# pcpgf-ova
Bovine serum albumin (BSA)	Jackson Immuno Research	Cat# 001-000-173
Normal Goat Serum Blocking Solution, 2.5%	Vector Laboratories	Cat# S-1012-50
Eosin Phloxine Alcoholic Working Solution	Poly Scientific	Cat# s176
Harris Modified Method Hematoxylin Stains	Fisher Chemical	Cat# SH26500D
Critical commercial assays		
CellTiter 96 Aqueous One Solution Cell Proliferation Assay (MTS)	Promega	Cat# G3582
Opal™ 520 Reagent Pack	PerkinElmer	Cat# FP1487001KT
Opal™ 570 Reagent Pack	PerkinElmer	Cat# FP1488001KT
ProLong™ Gold Antifade Mountant with DAPI	Invitrogen	Cat# P36931
Chromium I7 Multiplex Kit, 96 rxns	10x Genomics	Cat# PN-120262
BD Mouse IFN-γ ELISPOT Sets	BD Biosciences	Cat# 551083
VeriKine-HS Mouse IFN Beta ELISA Kit	PBL Assay Science	Cat# 42410
VeriKine Human IFN Beta ELISA Kit	PBL Assay Science	Cat# 414101
True-Nuclear™ Transcription Factor Buffer Set	BioLegend	Cat# 424401
EasySep™ Mouse $CD8^+$ T Cell Isolation Kit	STEMCELL Technologies	Cat# 19853
EasySep™ Human CD34 Positive Selection Kit II	STEMCELL Technologies	Cat# 18780
EasySep™ Mouse Steptavidin RapidSpheres™ Isolation Kit	STEMCELL Technologies	Cat# 19860
Clarity Max Western ECL Substrate	Bio-Rad	Cat# 1705062
ImmPRESS® HRP Horse Anti-Rabbit IgG Polymer Detection Kit	Vector Laboratories	Cat# MP-7401
e-Myco PCR Detection Kits	Bulldog Bio	Cat# 25233
Deposited data		
Single cell RNA-seq data and TCR sequencing data	This manuscript	GEO: GSE194166
Code for single cell RNA-seq analysis	This manuscript	https://doi.org/10.5281/zendo.5975533
Experimental Models: Cell Lines		
KP	Esra Akbay	N/A
KPL	Esra Akbay	N/A
A549 (Male, Adenocarcinoma, NSCLC)	ATCC	CRL-185
H2122 (Female, Adenocarcinoma, NSCLC)	John Minna and Adi Gazdar	RRID: CVCL_1531
Lenti-X 293T (Female, Kidney)	Takara	Cat# 632180
Experimental models: Organisms/strains		
C57BL/6J	UTSW breeding core	Cat# 000664
C57BL/6 (MPF)	Taconic Biosciences	Cat# B6NTac
B6.129S7-Rag1^{tm1Mom}/J mice	Jackson Laboratory	Cat# 002216
NSG-SGM3 mice	Jackson Laboratory	Cat# 013062
B6.129(C)-Batf3^{tm1Kmm}/J mice	Jackson Laboratory	Cat# 013755
C57BL/6-Tg (TcraTcrb)1100Mjb/J mice	Jackson Laboratory	Cat# 003831
Software and algorithms		
GraphPad Prism 9.0.0	GraphPad Software, Inc.	https://graphpad.com/scientific-software/prism/
CTL-ImmunoSpot® S6 Analyzer	Cellular Technology Limited	http://www.immunospot.com/ImmunoSpot-analyzers
CytExpert	Beckman Coulter, Inc	https://www.beckman.com/coulter-flow-cytometers/cytoflex/cytexpert

(*Continued on next page*)

Continued

REAGENT or RESOURCE	SOURCE	IDENTIFIER
BD FACSAria™ III System	BD Biosciences	https://www.bdbiosciences.com/en-us/instruments/research-instruments/research/cell/sorters/facsaria-iii
FlowJo	Tree Star Inc.	https://www.flowjo.com/solutions/flowjo
CellRanger (v3.1.0)	10x Genomics	https://support.10xgenomics.com/single-cell-gene-expression/software/pipelines/latest/installation
R (v4.0.2)	The R Foundation	https://www.r-project.org
Rstudio 1.3.1093	Rstudio	http://rstudio.com/products/rstudio/
Seurat (v.3.1.0, R package)	Stuart et al.[51]	https://github.com/satijalab/seurat
Monocle (v2, R package)	Qiu et al.[52], Trapnell et al.[53]	https://bustools.github.io/BUS_notebooks_R/monocle2.html
SingleR (v.1.3.8, R package)	Aran et al.[54]	https://github.com/dviraran/SingleR
ggplot2 (v3.2.1, R package)	Wickham[55]	https://ggplot2.tidyverse.org
Velocyto (v0.17.17, R package)	La Manno et al.[56]	http://velocyto.org
Uniform Manifold Approximation and Projection (UMAP)	McInnes and Healy[57]	https://github.com/lmcinnes/umap
Image Studio Lite	LiCor	http://licor.com/bio/image-studio-lite/
ZEN Digital Imaging	Zeiss	https://www.zeiss.com/microscopy/int/products/microscope-software/zen.html
NDP.View2	Hamamatsu Photonics	https://www.hamamatsu.com/us/en/product/type/U12388-01/index.html

RESOURCE AVAILABILITY

Lead contact

Further information and requests for resources and reagents should be directed to and will be fulfilled by the Lead Contact Rolf A. Brekken (rolf.brekken@utsouthwestern.edu).

Materials availability

This study did not generate new unique reagents.

Data and code availability

- Single-cell RNA-seq data have been deposited at GEO and are publicly available as of the date of publication. Accession numbers are listed in the key resources table.
- Microscopy data reported in this paper will be shared without restriction by the lead contact upon request.
- All original code has been deposited at Zenodo and is publicly available as of the date of publication. DOIs are listed in the key resources table.
- Any additional information required to reanalyze the data reported in this paper is available from the lead contact upon request.

EXPERIMENTAL MODEL AND SUBJECT DETAILS

Cell line and reagents

The KP and KPL cell lines were provided by Dr. Esra Akbay. The H2122 cell line was established by Drs. John Minna and Adi Gazdar at the NIH. A549 was obtained from ATCC. Lenti-X 293T cells were obtained from Takara (Cat# 632180). All cancer cell lines were grown in 5% FBS (ThermoFisher Scientific, Cat# 26140079) supplemented RPMI 1640 (Millipore Sigma, R8758). Cell lines were routinely tested using mycoplasma contamination kit (E-myco, Cat# 25233, Bulldog Bio) and cultured under 5% CO_2 at 37 ˚C. Primary BMDCs and T cells were isolated from mice as described below and cultured in with complete RPMI 1640 medium supplemented with 20 ng/ml recombinant mouse GM-CSF (rmGM-CSF) in a 10-cm dish.

Humanized mice and human cord blood sample processing

Humanized mice were established as previously described.[58] Briefly, 4-weeks-old NSG-SGM3 (Jackson Laboratories #013062) female recipient mice were treated with 100 cGy (X-ray irradiation with X-RAD 320 irradiator) whole body irradiation within 24 h prior to hematopoietic stem cells (HSCs) transplantation. Human HSCs were isolated from human cord blood by Ficoll (Cytiva, Cat# 17544203) density gradient centrifugation, followed with positive immunomagnetic selection with anti-human $CD34^+$ microbeads following the manufacturer's protocol (STEMCELL Technologies, cat# 18780). For transplantation, 1×10^6 HSCs were intravenously injected into recipient mice. Irradiated mice were orally administrated Sulfadiazine/Trimethoprim (Aurora Pharmaceutical LLC, Cat# 302) water for 14 days.[59,60] Twelve weeks after engraftment, humanized mice reconstituted with over 45% human $CD45^+$ cells were used for tumor studies. Human cord blood samples were obtained from UT Southwestern (UTSW) Parkland Hospital in compliance to the regulation and the use approval of human cord blood (STU 112010-047) at UTSW medical center. Sterile blood was obtained at the time of cesarean section from de-identified human umbilical cords that are normally discarded. The procedure is approved through a protocol exempt from informed consent as approved by the institutional review board of UTSW and the Office for Human Research Protections (OHRP) supported by the U.S. Department of Health and Human Services. To maintain anonymity, links between the donor's medical and social histories including fetal sex are not maintained.

Animal studies

Female C57BL/6J mice were purchased from the UT Southwestern breeding core or Taconic Biosciences. B6.129S7-$Rag1^{tm1Mom}$/J (*Rag1*$^{-/-}$), NOD.Cg-$Prkdc^{scid}$ $Il2rg^{tm1Wjl}$ Tg (CMV-IL3, CSF2, KITLG) 1Eav/MloySzJ (NSG-SGM3), B6.129S(C)-$Batf3^{tm1Kmm}$/J (*Batf3*$^{-/-}$), and C57BL/6J-Tg *(TcraTcrb)1100Mjb/J* (OT1 TCR transgenic mice) were purchased from Jackson Laboratory. All mice were housed by the UTSW Animal Resource Center at 68–79°F, 30–70% humidity, in individually ventilated cages, with no more than 5 mice per cage on 12 h on:off light:dark cycles. Mice were screened for and found free of MHV, Sendai virus, MPV, EDIM, MVM, PVM < TMEV-/GD-7, REO-3 virus, *Mycoplasma pulmonis*, pinworms, fur mites, LCMV, ECTRO, MAV, and K virus and had unrestricted access to RO chlorinated water and irradiated 2916 Teklab global diet (Envigo, Cat# 2916). Animal care and experiments were performed in complying with institutional and National Institutes of Health protocol and guidelines. This study has been approved by the Institutional Animal Care and Use Committee of the University of Texas Southwestern Medical Center (APN 2015–100921).

Clinical trial

Patients treated with bemcentinib and pembrolizumab combination therapy were enrolled in the BGBC008 clinical trial (BerGenBio ASA and Merck & Co., Inc., Kenilworth NJ, USA, NCT03184571). Information on demographics and characteristics of the three patients reported in this paper are given in Figure 6. The clinical demographics and characteristics of the remaining patients enrolled onto the trial are not yet available because the trial is ongoing. The data presented here represent preliminary findings on 3 of the trial participants. Fine-needle aspirate biopsies of target lesions were acquired from patients at screening immediately prior to enrollment in the study and preserved in formalin-fixed, paraffin-embedded (FFPE) tissue blocks. Patients were assessed for response according to RECIST 1.1 criteria at recurrent, scheduled scan intervals. The study was approved by all relevant institutions, including London Bridge Research Ethics Committee (UK), REC-South East (Norway), Drug Research Ethics Committee of the University Hospital Clinic of Barcelona (Spain), and MCW/FH Institutional Review Board #4, Medical College of Wisconsin (USA).

METHOD DETAILS

Cytotoxicity assays

For cell cytotoxicity analysis, 1000–2000 cells for corresponding cell lines were plated into each well of a 96-well plate. After 24 h, cells were treated with 4-fold serial dilutions of 8 different concentrations for 4 days. At the end time point of treatment, cell viabilities were determined using CellTiter 96 Aqueous One Solution Cell Proliferation Assay (MTS) (Promega, catalog# G3582) on a Molecular Devices SpectraMax 190 microplate reader under 450 nm wavelength. Dose-response curve was analyzed through GraphPad Prism.

OVA expressing cell line generation and characterization

The pCDH- EF1α-OVA plasmid (10 μg) was packaged with psPAX2 (5 μg) and pMD2.G (5 μg) into 2 million Lenti-X 293T cells (Takara, Cat# 632180) using FuGene6 (Promega, Cat# E2691) following the manufacturer's protocol. Virus containing medium was removed after 12 h and viral supernatant was collected every day for 3 days and filtered through 0.45 μm filter. For virus infection, viral supernatant was mixed with polybrene (6 μg/ml, Santa Cruz, Cat# sc-134220) and incubated with cells overnight. Infected cells were then plated into 96-well plates to identify single clones. For OVA expression characterization, cells were stimulated with IFNγ (10 IU/ml) overnight then stained with OVA257-264 peptide bound to H-2Kb antibody (eBioscience, Cat# 17-5743-82). 2-3 OVA expressing single clones with similar behavioral and growth pattern with parental KPL were pooled as KPL-OVA.

In Vitro Co-culture of Bone Marrow Dendritic Cells (BMDCs) and T cells

To generate BMDCs, a single-cell suspension of bone marrow cells were collected from tibias and femurs of C57BL/6J or Axl-/- mice as previously described.[61] Collected cells were cultured with complete RPMI 1640 medium supplemented with 20 ng/ml

recombinant mouse GM-CSF (rmGM-CSF) in a 10-cm dish. On day 3 and 6, equal amount of fresh media containing 20 ng/ml rmGM-CSF. The BMDCs were harvested from tissue culture suspension on day 7. For OVA specific $CD8^+$ T cells, the spleen and lymph nodes of OT1 transgenic mice were isolated with a negative $CD8^+$ T cell isolation kit (STEMCELL Technologies, Cat# 19853) following the manufacturer's instructions. For co-culture, 2×10^4 BMDCs were mixed with 2×10^5 $CD8^+$ T cells in the presence of 100 μg/mL OVA protein per well in a 96-well U-bottom plate. BGB324 at 40 nM was added. For *in vitro* IFNα receptor blockade, 10 μg of anti-mouse IFNAR-1 antibody (BioXCell, Cat# BE0241) or corresponding IgG (BioXCell, Cat# BE0083) was added. For *in vitro* IFNα stimulation, 0.5 ng/ml of recombinant IFNα was added. After 48hr, all the cells were collected for analysis by flow cytometry.

Immunoblots

For LKB1 protein detection, KP and KPL cells were cultured *in vitro*. Protein lysates were collected by washing cells with ice-cold PBS then incubated with a modified RIPA buffer (50 mM Tris, 150 mM NaCl, 0.1% SDS, 1% IGEPAL CA-630, 1% sodium deoxycholate, 2 mM $MgCl_2$, pH 8) with 1 unit/μl benzonase (MilliporeSigma, Cat# E1014), protease inhibitors (MilliporeSigma, Cat# P8340) and phosphatase inhibitors (MilliporeSigma, Cat# 4906845001) on ice for 15 min. Lysed cells were scraped and protein lysates were harvested. The concentration of total protein was quantified with Bradford Assay (Bio-Rad, Cat# 5000006) according to BSA standard (ThermoFisher Scientific, Cat# 23209). For each sample, 25 μg protein was mixed with loading dye and separated on a NuPAGE 4-20% TGX gel (Bio-Rad, Cat# 5671095) at 150V. Samples were transferred with the Trans-Blot Turbo RTA Mini Nitrocellulose transfer kit (Bio-Rad, Cat# 1704270) on a Trans-Blot Turbo Transfer System (Bio-Rad, Cat# 1704150) following manufacturer's recommended protocols. The membrane was blocked with 5% milk (Bio-Rad, Cat# 1706404XTU) dissolved in 0.1% in PBST. Membrane were probed with primary antibodies: LKB1 (1:1000, Cell Signaling Technology, Cat# 3047) and GAPDH (1:2500, Cell Signaling Technology, Cat# 5174), blots were incubated at 4 ˚C overnight. After washing with 0.1% PBST, the membranes were with secondary antibody (1:2000, Cell Signaling Technologies, Cat# 7074), washed and imaged with ECL substrate (Bio-Rad, Cat# 1705062), and visualized through a LiCor Odyssey Fc imaging system.

Tumor growth and treatment

For subcutaneous allografts, 1×10^6 cells in 100 μl phosphate buffered saline (PBS) were injected into right dorsal flanks of 6-8 wks old mice. For xenografts growing in humanized mice, 1.5×10^6 cells in 100 μl phosphate buffered saline (PBS) were injected into right dorsal flanks. Tumor bearing mice were randomly grouped into treatment groups when tumor volume was 100-150 mm^3. For each treatment group, 5 mice were assigned. 10 mg/kg PD-1 (BioXCell, Cat# BE0146) treatment was given intraperitoneally on day 0, day 4 and day 7 after treatment. Control animals were treated with 10 mg/kg rat IgG2a isotype control (BioX Cell, Cat# BE0089). BGB324 (50 mg/kg) was given through oral gavage twice daily. For tumor growth measurement, mice were treated for 3 weeks. For tumor microenvironment analysis, mice were treated for 7 days, harvested tumors from control and treatment groups were within 20% in size for TME analysis. For intratumoral IFNα receptor blocking, 50 μg IFNAR blocking (BioXCell, Cat# BE0241) antibody or control IgG (BioXCell, Cat# BE0083) were injected intratumorally 1 day before BGB324 + anti-PD-1 treatment started. IFNAR inhibition antibody was injected every other day. For Clophosome liposome depletion (FormuMax Scientific, Cat# F70101C-A), the amount of liposome recommended by corresponding COA was injected intraperitoneally into mice 1 day before therapy (BGB324 + anti-PD-1) treatment. After 5 days, a second liposome injection was performed. For recombinant IFNα, 200 ng of IFNα or PBS was injected intraperitoneally 14 days after tumor inoculation. Tumor volumes were measured by length (a), width (b) and height (h) in every 3 days and calculated as tumor volume = abh.

IFN-γ enzyme-linked immunosorbent spot assay (ELISPOT)

KPL-OVA (1×10^6) cells were injected subcutaneously on the right flank of 6-8 weeks old C57BL/6J mice purchased from Taconic Biosciences. Seven days after treatment started, tumors were harvested and digested into single cells. For each well of a 96-well plate, tumor infiltrated lymphocytes (TILs) were isolated from 3×10^5 digested single cells by biotin labeling (BioLegend, Cat# 101304) followed by negative immunomagnetic selection (STEMCELL Technologies, Cat# 19860). Isolated TILs were cultured in RPMI 1640 medium supplemented with 10% fetal bovine serum, 2 mmol/l L-glutamine, 100 U/ml penicillin, and 100 μg/ml streptomycin. For antigen specific $CD8^+$ T cell stimulation, 1 μg/ml of SIINFEKL peptide ($OVA_{257-264}$) or control RAHYNIVTF (E7) peptide were added. After 48 h of incubation, IFN-γ production was determined with an IFN-γ ELISPOT assay kit according to the manufacturer's protocol (BD Biosciences, Cat# 551083). The visualized spots were enumerated with the CTL-ImmunoSpot® S6 Analyzer (Cellular Technology Limited) and normalized based on digested tumor cell counts.

Enzyme-Linked Immunosorbent Assay (ELISA)

Co-culture of BMDCs with irradiated tumor cells to detect type I IFN was performed as previously described.[45] BMDCs (2×10^5) were co-cultured with 40g irradiated KPL cells (2×10^6), with or without BGB324 treatment (40 nM). After 24 h, cell supernatant was collected for analysis. The concentration of IFNβ was measured by VeriKine-HS Mouse IFN Beta Serum ELISA kit (PBL Assay Science, Cat# 42410), or VerKine Human IFN Beta ELISA kit (PBL Assay Science, Cat# 414101) in accordance with the manufacturer's instructions. Finally, the plates were visualized by adding 100 μL of TMB solution and read at 450 nm using the SPECTROstarNano (BMG LABTECH).

Single cell preparation for flow sorting and flow cytometry

Tumor tissues were excised and digested with 2 mg/mL Collagenase A (Sigma, Cat# SCR136) and 1 mg/ml DNase I (Roche, Cat#11284932001) under 37 °C, 150 rpm shaking speed for 45 min. Digested materials then were transferred to a 70 μm cell strainer to remove clumped cells. Digested cells were washed twice with FACs buffer and ready for downstream analysis.

Library preparation and construction for scRNA-seq and scTCR-seq

KP (n = 10) and KPL (n = 10) allografts were harvested 14 days after subcutaneous implantation (average tumor size ~200 mm^3). For each sample, individual tumors harvested from different mice were pooled with live $CD45^+$ $CD3^-$: $CD45^+$ $CD3^+$ cells sorted and mixed back as 1:1 ratio. Single cell libraries and TCR libraries were generated with Chromium Single Cell V(D)J Reagent Kit (10x Genomics, PN-10000006, PN-10000009, PN-1000071) following per manufacturer's instruction. Pooled control group tumors from KPL tumors were also used to compare with KP tumors.

Flow cytometry analysis

Total number of digested cells for each tumor sample was counted, and a single cell suspension of 1.5 million of cells was used to perform analysis. Samples were incubated with anti-FcγIII/II receptor (clone 2.4G2) for 15 min at 4°C to block potential non-specific binding of conjugated antibodies. Indicated antibodies were incubated with digested tumor samples for 30 min at 4°C. Fixable viability Dye eFluor 506 (eBioscience, Cat# 65-0866-18) was used to exclude the dead cells. Ki67 and TCF1 were stained intracellularly using True-Nuclear transcription factor buffer set (BioLegend, Cat# 424401) following the manufacturer's instructions. Data were collected on CytoFLEX flow cytometer (Beckman Coulter, Inc) and analyzed by using FlowJo (Tree Star Inc., Ashland, OR) software.

Hematoxylin and Eosin (H&E) staining

Formalin fixed paraffin embedded slides (5 μm) were deparaffinized with xylene, ethanol, and deionized water. Slides were then stained with hematoxylin (Fisher Chemical, Cat# SH26500D) and washed/destained with acid ethanol. Eosin (Poly Scientific, Cat# s176) was then applied to slides and then washed with 95% ethanol. Stained slides were dehydrated with ethanol and xylene.

Multiplex immunohistochemistry (IHC)

Multiplex immunohistochemistry (IHC) was performed as previously described.[62] Briefly, slides were warmed in a 60°C oven for 10 min followed by deparaffinization and rehydration. Before antigen retrieval, slides were fixed in 10% neutral buffered formalin for 30 min followed by a PBS wash. Antigen retrieval was performed in antigen retrieval buffer (10 mM Tris-HCl, 1 mM EDTA with 10% glycerol [pH 9]) at 110°C for 17 min (~4–5ψ). Slides were cooled down to room temperature and washed once with PBS. Tissue sections were blocked with 2.5% goat serum (Vector Laboratories, S-1012) for 30 min followed by incubation with primary antibody (CD8, 1:2000; Cell Signaling, 98941) overnight at 4°C. Slides were washed three times for 5 min in PBST (0.05% Tween 20 and 2 mM EDTA) and incubated with HRP conjugated secondary anti-rabbit Antibody (ImmPRESS; Vector Laboratories, MP-7401) for 30 min on a shaker. Slides were then washed three times for 5 min in PBST. For developing the fluorescence signal, TSA detection system (PerkinElmer) was used. We used Opal 520 to stain for CD8. Multiplex staining was performed by stripping the previous antibody in 10 mM citrate buffer (pH 6.2) plus 10% glycerol at 110°C for 2 min before blocking and probing with the next primary Ab: TCF1/7 (1:1000, Cell Signaling). Following similar steps from the first round of staining, slides were developed with Opal570 to stain for TCF1/7. Slides were counter-stained with DAPI and then cover-slipped using Pro-Long Gold mount (No. P36931; Life Technologies). Slides were scanned at 20X using the Zeiss Axioscan.Z1 (Whole Brain Microscopy Facility, UT Southwestern). DAPI, AF488 (for Opal520) and AF555 (for Opal570) channels were used to acquire images.

Tissue microarrays immunohistochemistry staining

Tissue microarrays (TMAs) were generated with resected Non-small cell lung carcinoma tumor samples (TMA3). IHC staining was performed on 4-μm thickness TMAs sections in a Leica Bond RX automated strainer (Leica Biosystems). Antigen retrieval was performed with Bond ER Solution #1 (Leica Biosystems) equivalent to citrate buffer, pH 9.0 for 20 min at 100°C. The sections were incubated with anti-AXL antibody (rabbit monoclonal, Cell Signaling clone C89E7); 1:300 dilution (1 μg/ml). The antibody was detected using Bond Polymer Refine Detection kit (Leica Biosystems) with diaminobenzidine (DAB) as chromogen. All the slides were counterstained with hematoxylin, dehydrated, and cover slipped. Tonsil and normal colon sections were used as external positive controls. Each case was analyzed using standard microscopy by two pathologists (LS, SH) in immune cells and reported as percentage of the tumor area occupied with immune cell with cytoplasmic and/or membrane expression.

QUANTIFICATION AND STATISTICAL ANALYSIS

Statistical analysis

All data were processed and analyzed through GraphPad Prism statistical software (version 9.0.0, GraphPad Software Inc.) and shown as mean ± SD. One-way ANOVA with Tukey's multiple comparison test was used to compare tumor growth and MFIs with more than 2 treatment groups, and unpaired two-tailed *t* tests was used to analyze the other data. *Chi*-square test was used for

IHC image quantification analysis. A value of $p < 0.05$ was considered statistically significant (*$p < 0.05$, **$p < 0.01$, ***$p < 0.001$ and ****$p < 0.0001$).

Flow ytometry cell number normalization

The absolute cell number of designated cell populations were calculated based on the percentage of infiltrated cells, normalized with absolute cell number of harvested tumor and measured tumor size.

scRNA-seq and scTCR-seq data processing

Sequenced scRNA-seq samples were processed through Cellranger pipelines (v3.1.0). Cellranger count was used to align reads to mouse reference genome (mm10, 2020-A, from 10x Genomics) and generate single cell feature counts for single library. For scTCR-seq data, TCR reads were aligned to reference genome and TCR annotation was performed using the 10x cellranger vdj pipeline with provided reference (cellranger-vdj-GRCm38-alts-ensembl-4.0.0). Overall, 94% of T cells in scRNA-seq data were assigned a TCR and more than 70% had at least one full-length productive CDR3 for TRB. Cellranger aggr were applied next to aggregate each sample library for grouped analysis with same effective sequencing depth. Seurat (3.2.1) package was used for multiple library data integration and downstream analysis including singlet filtration, dimensional reduction, data scaling, clustering and markers identification.[51]

Annotation of cell clusters and data visualization

To identify the cell clusters, we annotated the cell cluster identities based on (1) well-studied marker genes of different immune cell types were in the top rank of differential expressed genes and assign the identity to the most likely cell populations; (2) unbiased cell population identification package singleR (v1.3.8).[54] For visualization, we applied the uniform manifold approximation and projection (UMAP) to visualize cell clusters.[63] For $CD8^+$ T cells sub-clustering, we split the $CD3^+$ T cells according to the mutually exclusive expression of CD4 (CD4> 1 and CD8A< 1) and CD8A (CD4<1 and CD8A>1) genes based on their normalized expression. $CD8^+$ T cells were then sub-clustered and annotated based on their highly enriched genes with well-known markers.[32]

Differential expression analysis

CD8a expressing T cells were subset and analyzed for differential expressed gene among KP and KPL samples using Seurat package (3.2.1). Then differential expressed genes were ranked based on log Fc value, with p value >0.01 highlighted in grey, and p value <0.01 highlighted in red. Then the graph was plotted using ggplot 2 package.

Characterization of sample enrichment and state transition of T cell clusters

To measure the enrichment of specific T cell clusters in each sample induced by different treatment, we calculated the ratio of observed to expected cell number for each T cell cluster. Chisq-squared test was applied to test whether the distribution of T cell clusters across different samples was significantly deviates from random expectations. The extent of deviation for each combination of T cell cluster and sample is quantified by the Ro/e value:

$$R_{o/e} = \frac{N_o}{N_e}$$

where N_o is the observed number cell for a given sample and cluster combination, while the *Ne* is the expected number obtained from Chi-square test. Theoretically, $R_{o/e} > 1$ suggests that cells identified in the given cluster shows higher frequency than random expectations for the analyzed sample, and vice versa. The normalization and scaling of the shared clonotypes between CD8 T cell clusters was performed and analyzed based on previous publication.[32] The shared clone scores were also scaled with a constant of 10,000.

RNA velocity analysis

To predict the future status and direction of each cells transitioning, RNA velocity analysis was performed.[56] Un-spliced mRNAs were generated as a loom file for each individual sample output from Cell Ranger and RNA velocity was calculated based on velocyto (v0.17.17, Linux R package). Generated loom files were then merged and projected to UMAP coordinates of single cells.

ADDITIONAL RESOURCES

This paper reports preliminary data from a clinical trial (NCT03184571).